Flavon signatures at the HL-LHC

M. A. Arroyo-Ureña,[1,2,*] Amit Chakraborty,[3,†] J. Lorenzo Díaz-Cruz,[1,2,‡] Dilip Kumar Ghosh,[4,§] Najimuddin Khan,[5,‖] and Stefano Moretti[6,7,¶]

[1]*Facultad de Ciencias Físico-Matemáticas, Benemérita Universidad Autónoma de Puebla, C.P. 72570, Puebla, Mexico*
[2]*Centro Interdisciplinario de Investigación y Enseñanza de la Ciencia (CIIEC), Benemérita Universidad Autónoma de Puebla, C.P. 72570, Puebla, Mexico*
[3]*Department of Physics, School of Engineering and Sciences, SRM University AP, Amaravati, Mangalagiri 522240, India*
[4]*School of Physical Sciences, Indian Association for the Cultivation of Science, 2A and 2B Raja S.C. Mullick Road, Kolkata 700032, India*
[5]*Harish-Chandra Research Institute, A CI of Homi Bhabha National Institute, Chhatnag Road, Jhunsi, Prayagraj 211019, India*
[6]*School of Physics and Astronomy, University of Southampton, Highfield, Southampton SO17 1BJ, United Kingdom*
[7]*Department of Physics and Astronomy, Uppsala University, Box 516, SE-751 20 Uppsala, Sweden*

(Received 17 July 2023; accepted 20 October 2023; published 14 November 2023)

The detection of a single Higgs boson at the Large Hadron Collider (LHC) has allowed one to probe some properties of it, including the Yukawa and gauge couplings. However, in order to probe the Higgs potential, one has to rely on new production mechanisms, such as Higgs pair production. In this paper, we show that such a channel is also sensitive to the production and decay of a so-called 'flavon' field (H_F), a new scalar state that arises in models that attempt to explain the hierarchy of the Standard Model (SM) fermion masses. Our analysis also focuses on the other decay channels involving the flavon particle, specifically the decay of the flavon to a pair of Z bosons ($H_F \to ZZ$) and the concurrent production of a top quark and charm quark via the $\phi \to tc$ decays ($\phi = H_F, A_F$), having one or more leptons in the final states. In particular, we show that, with 3000 fb^{-1} of accumulated data at 14 TeV (the Run 3 stage) of the LHC an heavy flavon H_F with mass $M_{H_F} \simeq 2m_t$ can be explored with 3σ–5σ significance through these channels.

DOI: 10.1103/PhysRevD.108.095026

I. INTRODUCTION

The discovery of a Higgs boson [1–3] with mass $M_h = 125.5$ GeV has provided a firm evidence for the mechanism of electroweak symmetry breaking (EWSB) based on a Higgs potential [4,5] pointing towards the minimal realization of it that defines the Standard Model (SM). So far, the corresponding studies have relied on the four standard single Higgs production mechanism, i.e., gluon-gluon fusion, vector boson fusion, Higgs-strahlung and associated production with top-quark pairs (see Ref. [6]), which have permitted to extract the Higgs boson couplings with quarks (b and t), leptons (τ and μ) and gauge bosons (W and Z) as well as the effective interaction with photon and gluon pairs. However, there still remains the task of probing the Higgs self-coupling. Moreover, we still do not understand the origin of the Yuwaka couplings, the flavor coupling. The Higgs boson pair (hh) production serves as a direct means of investigating the self-interactions of the Higgs boson, which play a crucial role in determining the Higgs potential of the SM. Additionally, the magnitude of the hh production rate is directly proportional to the square of this self-coupling. Within the SM, the nonresonant production of Higgs boson pairs represents the only direct method for measuring the Higgs boson self-coupling. Nonetheless, due to the limited size of the cross section, accurately determining this coupling presents a significant challenge. Next-to-leading-order effects help somewhat to improve the situation [7–9]. The production of SM-like Higgs boson pairs at the LHC provides a valuable avenue to probe various scenarios

*marco.arroyo@fcfm.buap.mx
†amit.c@srmap.edu.in
‡jldiaz@fcfm.buap.mx
§tpdkg@iacs.res.in
‖najimuddinkhan@hri.res.in
¶s.moretti@soton.ac.uk; stefano.moretti@physics.uu.se

Beyond the SM (BSM) that contain particles having couplings with the Higgs boson [10–12]. These new particles could be (pseudo)scalars, fermions and gauge bosons. Thus di-Higgs production offers insights into the properties of the Higgs boson itself and can potentially shed light on the Higgs self-interactions as well as its interactions with other particles in the model. For example, in the dominant production mode for di-Higgs bosons at the LHC, through fusion of gluons, mediated by top-quark loops that couple to both gluons and Higgs boson. Any additional heavy colored fermions that couple with the Higgs boson can contribute to the di-Higgs production mode too. Similarly, in some BSM scenarios, Higgs production can be associated with other colored particles in the loops, such as squarks in Supersymmetry.

Studies have shown that, in all generality, in scenarios with an extended Higgs sector, new heavy resonances, supersymmetric theories, effective field theories with modified top Yukawa coupling, etc., di-Higgs (hh) and di-gauge boson (W^+W^-/ZZ) production receives additional BSM contributions along with the SM ones [12–51]. These effects make the study of these two production processes particularly interesting then and, at the same time, also very challenging. However, the possibility to produce Higgs and gauge bosons pairs in the decay of a new heavy particle that belongs to the spectrum of those models offers some hope to achieve detectable signals at current and future colliders. It is also to be noted that flavor-violating Higgs decays, i.e., those violating the conservation of flavor quantum numbers [52] can be possible. This phenomenon is of great interest as it can provide evidence for BSM physics and shed light on the origin of flavor mixing and hierarchy in the fermion sector. The study of flavor-violating Higgs decays thus offers a unique opportunity to explore new physics and deepen our understanding of fundamental interactions in the Universe [53–55].

Specifically, we will study the interactions of the discovered Higgs boson with the so-called 'flavon' field H_F which appears in models that attempt to explain the hierarchy of quark and lepton masses using the Froggatt-Nielsen (FN) mechanism [56–58]. This mechanism assumes that, above some scale M_F roughly corresponding to the flavon mass, there is a symmetry, perhaps of Abelian-type $U(1)_F$, with the SM fermions being charged under it, which then forbids the appearance of Yukawa couplings at the renormalizable level. However, Yukawa matrices can arise through nonrenormalizable operators. The Higgs spectrum of these models includes a light H_F state, which could mix effectively with the SM Higgs boson when the flavor scale is of the order 1 TeV or lower. Recently, the phenomenology of Higgs vs flavon interactions at particle colliders has been the focus of some attention [59–66]. In particular, within this framework, it is possible to have a coupling of this new scalar with Higgs and gauge bosons pairs, which can then provide interesting signals to be searched for at the LHC. Another characteristic to highlight is the emergence of flavor changing neutral currents (FCNCs) mediated by the flavon, which allows the $H_F \to tc$ decay at tree level. Our study could thus not only serve as a strategy for the flavon search, but it can also be helpful to assess the order of magnitude of flavor violation mediated by such a particle, which is an indisputable signature of BSM physics.

In this paper, we are interested in studying the detection of the flavon signal emerging from the production and decay processes $pp \to H_F \to hh(h \to \gamma\gamma, h \to b\bar{b})$, $pp \to H_F \to ZZ(Z \to \ell\overline{\ell})$ and the FCNC process $pp \to H_F \to tc(t \to \ell\nu_\ell b)$ at future stages of the LHC, namely, Run 3 and the high-luminosity LHC (HL-LHC) [67,68]. In this analysis, we do not take into consideration the $pp \to H_F \to hh(h \to \tau^+\tau^-, h \to b\bar{b})$ channel, which has the potential to be competitive with our selected signal. We have opted to exclude this channel from the current study and instead reserve it for a future publication. Additionally, we will not be presenting other channels such as $pp \to H_F \to hh(h \to b\bar{b})$ and $pp \to H_F \to WW(W \to \ell\nu_\ell)$ because these channels are highly suppressed by large SM backgrounds.

The ATLAS and CMS Collaborations at the LHC have already performed several studies of nonresonant di-Higgs and diboson(W/Z) production with various possible final states using both Run 1 and the Run 2 dataset. None of these searches have observed a statistically significant excess over the SM background, therefore, upper limits on the di-Higgs production cross section are placed [69–81]. We focus here on the '2γ plus $2b$-jets', '2 pairs of same flavor opposite sign (SFOS) leptons' and '2 jets plus a charged lepton with its neutrino' (with one of the jets labeled as a b-jet) signatures. These particular (and comparatively clean) final states are obtained through $pp \to H_F \to hh$, $pp \to H_F \to ZZ$ and $pp \to H_F \to tc$ production followed by $h \to \gamma\gamma$, $h \to b\bar{b}$, $Z \to \ell\overline{\ell}$ and $t \to \ell\nu_\ell b$ decays. We will show that these channels have large significances in specific parameter space regions in the context of the LHC operated at $\sqrt{s} = 14$ TeV of energy with integrated luminosity 3000 fb^{-1}. Besides these future energies and luminosities, we also present our results based on the data set accumulated to date, i.e., with a luminosity of 139 fb^{-1} at the 13 TeV LHC (Run 2).

The advocated signature of SM di-Higgs (hh) and diboson (ZZ) processes have been explored earlier in the literature, albeit in different scenarios [12–45], while the processes tackled here, $pp \to H_F \to hh(h \to \gamma\gamma, h \to b\bar{b})$ and $pp \to H_F \to ZZ(Z \to \ell\overline{\ell})$ and $pp \to \phi \to tc$ in the context of the present model have not been discussed in any depth [59–64]. Our analysis of these final states give promising results as a discovery channel for a heavy CP-even H_F boson in the aforementioned FN framework. In order to prove this, we first choose three sets of reference points for three heavy Higgs masses 800 GeV, 900 GeV, and 1000 GeV. A signal region (a set of different kinematic cuts) is then defined to maximize signal significances in the

presence the SM backgrounds having the same final state. In our cut-based analysis, we further use the same signal region for different combinations of the singlet scalar vacuum expectation value (VEV) v_s and heavy Higgs mass M_{H_F} to compute the signal significances. The latter are only mildly affected (at the 5–10% level) by incorporating a realistic 5% systematic uncertainty in the SM background estimation. We find a large number of signal events that have significances exceeding 2σ and they can be explored with 3000 fb^{-1} of data at LHC runs using $\sqrt{s} = 14$ TeV.

The rest of the paper is organized as follows. In Sec. II, we present the details of the model and derive expressions for the masses and relevant interaction couplings for all the particles. Afterwards, we introduce the constraints acting on it from both the theoretical and experimental side in Sec. III. Section IV is focused on the analysis of the signals arising from the decay of the flavon. Finally, we conclude in Sec. V.

II. THE MODEL

We now focus on some relevant theoretical aspects of what we will refer to as the FN singlet model (FNSM). In Ref. [82], a comprehensive theoretical analysis of the Higgs potential therein is presented along with the constraints on the parameter space from the Higgs boson signal strengths and the oblique parameters, including presenting a few benchmark scenarios amenable to phenomenological investigation. (See Ref. [83] for the effects of lepton flavor violation (LFV).)

A. The scalar sector

The scalar sector of this model consists of the SM Higgs doublet Φ ane and one SM singlet complex FN scalar S_F. In the unitary gauge, we parametrize these fields as

$$\Phi = \begin{pmatrix} 0 \\ \frac{v+\phi^0}{\sqrt{2}} \end{pmatrix}, \tag{2.1}$$

$$S_F = \frac{(v_s + S_R + iS_I)}{\sqrt{2}}, \tag{2.2}$$

where v and v_s represent the VEVs of the SM Higgs doublet and FN singlet, respectively. The scalar potential should be invariant under the FN $U(1)_F$ flavor symmetry. Under this symmetry, the SM Higgs doublet H and FN singlet S_F transform as $\Phi \to \Phi$ and $S_F \to e^{i\theta} S_F$, respectively.

In general, such a scalar potential admits a complex VEV, $\langle S_F \rangle_0 = \frac{v_s}{\sqrt{2}} e^{i\xi}$, but in this work we consider the special case in which the Higgs potential is CP-conserving, by setting the phase $\xi = 0$. Such a CP-conserving Higgs potential is then given by

$$V_0 = -\frac{1}{2} m_1^2 \Phi^\dagger \Phi - \frac{1}{2} m_2^2 S_F^* S_F + \frac{1}{2} \lambda_1 (\Phi^\dagger \Phi)^2 + \lambda_2 (S_F^* S_F)^2 + \lambda_3 (\Phi^\dagger \Phi)(S_F^* S_F). \tag{2.3}$$

The $U(1)_F$ flavor symmetry of this scalar potential is spontaneously broken by the VEVs of the spin-0 fields (Φ, S_F) and this leads to a massless Goldstone boson in the physical spectrum. In order to give a mass to it, we add the following soft $U(1)_F$ breaking term to the potential,

$$V_{\text{soft}} = -\frac{m_3^2}{2} (S_F^2 + S_F^{*2}). \tag{2.4}$$

The full scalar potential is thus,

$$V = V_0 + V_{\text{soft}}. \tag{2.5}$$

The presence of the λ_3 term allows mixing between the flavon and the Higgs fields after both the $U(1)_F$ flavor and EW symmetry breaking and contributes to the mass parameters for both the flavon and Higgs field, as can be seen below. The soft $U(1)_F$ flavor symmetry breaking term V_{soft} is responsible for the pseudoscalar flavon (S_I) mass. Once the minimization conditions for the potential V are applied, we obtain the following relations between the parameters of V:

$$m_1^2 = v^2 \lambda_1 + v_s^2 \lambda_3, \tag{2.6}$$

$$m_2^2 = -2m_3^2 + 2v_s^2 \lambda_2 + v^2 \lambda_3. \tag{2.7}$$

All the parameters of the scalar potential are real and therefore the real and imaginary parts of V do not mix. The CP-even mass matrix can be written in the (ϕ_0, S_R) basis as

$$M_S^2 = \begin{pmatrix} \lambda_1 v^2 & \lambda_3 v v_s \\ \lambda_3 v v_s & 2\lambda_2 v_s^2 \end{pmatrix}. \tag{2.8}$$

The corresponding mass eigenstates are obtained via the standard 2×2 rotation,

$$\phi^0 = \cos\alpha h + \sin\alpha H_F, \tag{2.9}$$

$$S_R = -\sin\alpha h + \cos\alpha H_F, \tag{2.10}$$

with α a mixing angle. Here h is identified with the SM-like Higgs boson with mass $M_h = 125.5$ GeV whereas the mass eigenstate H_F is the CP-even flavon. The corresponding CP-odd flavon $A_F \equiv S_I$ will have a mass such that $M_{A_F}^2 = 2m_3^2$. Both H_F and A_F are considered to be heavier than h. In this model, we will work with the mixing angle α and physical masses M_h, M_{H_F}, and M_{A_F}, which are related to the quartic couplings of the scalar potential in Eq. (2.3) as follows:

TABLE I. Tree-level couplings of the SM-like Higgs boson h and the flavons H_F and A_F to fermion and gauge boson pairs in the FNSM. Here, $r_s = v/\sqrt{2}v_s$.

Vertex (ϕXX)	Coupling constant ($g_{\phi}XX$)
$hf_i\bar{f}_j$	$\frac{c_\alpha}{v}\tilde{M}^f_{ij} - s_\alpha r_s \tilde{Z}^f_{ij}$
$H_F f_i \bar{f}_j$	$\frac{s_\alpha}{v}\tilde{M}^f_{ij} + c_\alpha r_s \tilde{Z}^{f_{ij}}$
$A_F f_i \bar{f}_j$	$i r_s \tilde{Z}^{f_{ij}}$
hZZ	$i\frac{gM_Z}{c_W}c_\alpha$
hWW	$igM_W c_\alpha$
$H_F ZZ$	$i\frac{gM_Z}{c_W}s_\alpha$
$H_F WW$	$igM_W s_\alpha$
$H_F hh$	$-i\{c_\alpha^3\lambda_3 v_s + c_\alpha^2 s_\alpha v(3\lambda_1 - 2\lambda_3) - 2c_\alpha s_\alpha^2 v_s(\lambda_3 - 3\lambda_2) + \lambda_3 s_\alpha^3 v\}$ $\equiv -i\{c_\alpha s_\alpha(3M^2_{A_F}s_\alpha v + (M^2_{H_F} + 2M_h^2)(s_\alpha v + c_\alpha v_s))\}/(vv_s)$
$A_F hh$	0
$A_F ZZ$	0

$$\lambda_1 = \frac{\cos\alpha^2 M_h^2 + \sin\alpha^2 M^2_{H_F}}{v^2},$$
$$\lambda_2 = \frac{M^2_{A_F} + \cos\alpha^2 M^2_{H_F} + \sin\alpha^2 M_h^2}{2v_s^2},$$
$$\lambda_3 = \frac{\cos\alpha\sin\alpha}{vv_s}(M^2_{H_F} - M_h^2). \tag{2.11}$$

We consider the mixing angle α, the FN singlet VEV v_s and its (pseudo)scalar field masses M_{H_F,A_F} as free parameters in this work.

B. The Yukawa sector

The effective $U(1)_F$ invariant Yukawa Lagrangian, *á la* FN, is given by [58]

$$\mathcal{L}_Y = \rho^d_{ij}\left(\frac{S_F}{\Lambda_F}\right)^{q^d_{ij}}\bar{Q}_i d_j\tilde{\Phi} + \rho^u_{ij}\left(\frac{S_F}{\Lambda_F}\right)^{q^u_{ij}}\bar{Q}_i u_j\Phi + \rho^\ell_{ij}\left(\frac{S_F}{\Lambda_F}\right)^{q^l_{ij}}\bar{L}_i\ell_j\Phi + \text{H.c.}, \tag{2.12}$$

where $\rho^{u/d/\ell}$ are dimensionless couplings seemingly of order one. This will lead to Yukawa couplings once the $U(1)_F$ flavor symmetry is spontaneously broken. The integers q^f_{ij} $(f = u, d, \ell)$ are the combination of $U(1)_F$ charges of the respective fermions. In order to generate the Yukawa couplings, one spontaneously breaks both the $U(1)_F$ and EW symmetries. In the unitary gauge one can make the following first-order expansion of the neutral component of the heavy flavon field S_F around its VEV v_s:

$$\left(\frac{S_F}{\Lambda_F}\right)^{q_{ij}} = \left(\frac{v_s + S_R + iS_I}{\sqrt{2}\Lambda_F}\right)^{q_{ij}} \simeq \left(\frac{v_s}{\sqrt{2}\Lambda_F}\right)^{q_{ij}}\left[1 + q_{ij}\left(\frac{S_R + iS_I}{v_s}\right)\right], \tag{2.13}$$

which leads to the following fermion couplings after replacing the mass eigenstates in $\mathcal{L}_Y$:

$$\mathcal{L}_Y = \frac{1}{v}[\bar{U}M^u U + \bar{D}M^d D + \bar{L}M^\ell L](c_\alpha h + s_\alpha H_F) + \frac{v}{\sqrt{2}v_s}[\bar{U}_i\tilde{Z}^u_{ij}U_j + \bar{D}_i\tilde{Z}^d_{ij}D_j + \bar{L}_i\tilde{Z}^\ell_{ij}L_j] \times(-s_\alpha h + c_\alpha H_F + iA_F) + \text{H.c.}, \tag{2.14}$$

where we define $\sin\alpha \equiv s_\alpha$ and $\cos\alpha \equiv c_\alpha$. Here, M^f stands for the diagonal fermion mass matrix while the intensities of the Higgs-flavon couplings are encapsulated in the $\tilde{Z}^f_{ij} = U^f_L Z^f_{ij} U^{f\dagger}_L$ matrices. In the flavor basis, the Z^f_{ij} matrix elements are given by

$$Z^f_{ij} = \rho^f_{ij}\left(\frac{v_s}{\sqrt{2}\Lambda_F}\right)^{q^f_{ij}} q^f_{ij}, \tag{2.15}$$

which remains nondiagonal even after diagonalizing the mass matrices, thereby giving rise to FV scalar couplings. In addition to the Yukawa couplings we also need the ϕVV $(V = W, Z)$ couplings for our calculation which can be extracted from the kinetic terms of the Higgs doublet and complex singlet. In Table I we show the coupling constants for the interactions of the SM-like Higgs boson and the flavon to fermions and gauge bosons.

III. CONSTRAINTS ON THE FNSM PARAMETER SPACE

In order to perform a realistic numerical analysis of the signals analyzed in this work, i.e., $pp \to H_F \to hh(h \to b\bar{b}, h \to \gamma\gamma)$, $pp \to H_F \to ZZ(Z \to \ell\bar{\ell})$, and $pp \to H_F \to tc(t \to \ell\nu_\ell b)$ (see Fig. 1), we need to constrain the free FNSM parameters, i.e., (i) the mixing angle α of the real components of the doublet Φ and the FN singlet S, (ii) FN singlet VEV v_s, (iii) the heavy scalar (pseudo) field masses M_{H_F,A_F}, (iv) the diagonal $\tilde{Z}^u_{33} \equiv \tilde{Z}_{tt}$, $\tilde{Z}^u_{22} \equiv \tilde{Z}_{bb}$

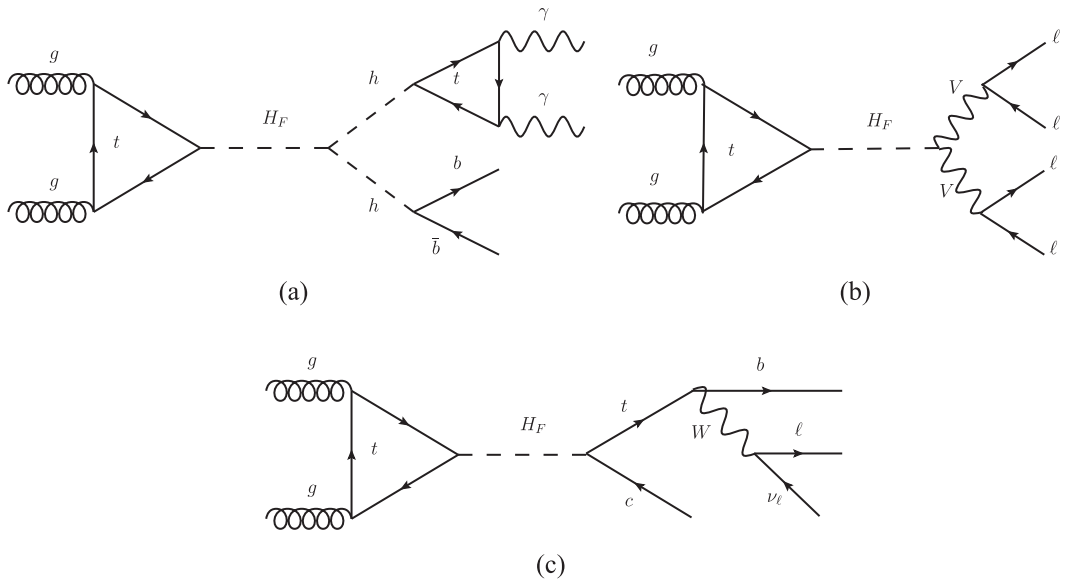

FIG. 1. Representative Feynman diagram of the signal: (a) $gg \to H_F \to hh(h \to b\bar{b}, h \to \gamma\gamma)$, (b) $gg \to H_F \to ZZ(Z \to \ell\bar{\ell})$ and (c) $pp \to \phi \to tc(t \to \ell\nu_\ell b)$.

and the nondiagonal $\tilde{Z}^u_{32} \equiv \tilde{Z}_{tc}$ matrix elements which will be used to evaluate both the production cross section of the flavon H_F and the decay of the Higgs boson to a pair of b quarks; all of which have an impact on the upcoming calculations. These parameters are constrained by various kinds of theoretical bounds like absolute vacuum stability, triviality, perturbativity and unitarity of scattering matrices and different experimental data, chiefly, LHC Higgs boson coupling modifiers, null results for additional Higgs states plus the muon and electron anomalous magnetic (dipole) moments Δa_μ and Δa_e, respectively. The various LFV processes $\tau \to 3\mu$, $\mu \to 3e$, $\tau \to \mu\gamma$, $\mu \to e\gamma$, $B^0_s \to \mu^+\mu^-$ and the total decay width of the Higgs boson (Γ^h_T) are also modified in the presence of these new Yukawa couplings, so they have also been tested against available data. In the following, we discuss the various constraints on the model parameters in turn.

A. Stability of the scalar potential

The absolute stability of the scalar potential in Eq. (2.3) requires that the potential should not become unbounded from below, i.e., it should not approach negative infinity along any direction of the field space (h, H_F, A_F) at large field values. Since in this limit the quadratic terms in the scalar potential are negligibly small as compared to the quartic terms, the absolute stability conditions are [84]

$$\lambda_1(\Lambda) > 0, \qquad \lambda_2(\Lambda) > 0 \quad \text{and} \quad \lambda_3(\Lambda) + \sqrt{2\lambda_1(\Lambda)\lambda_2(\Lambda)} > 0, \tag{3.1}$$

wherein these quartic couplings are evaluated at a scale Λ using renormalization group evolution (RGE) equations. If the scalar potential in Eq. (2.3) has a metastable EW vacuum, then these conditions are modified [84]. One can then use Eq. (2.11) to translate these limits into those on the free parameters such as scalar fields' mass and mixing angles.

B. Perturbativity and unitarity constraints

To ensure that the radiatively improved scalar potential of the FNSM remains perturbative at any given energy scale, one must impose the following upper bounds on the quartic couplings:

$$|\lambda_1(\Lambda), \lambda_2(\Lambda), \lambda_3(\Lambda)| \leq 4\pi. \tag{3.2}$$

The quartic couplings in the scalar potential of our scenario are also severely constrained by the unitarity of the scattering matrix (S-matrix). At very large field values, one can get the S-matrix by using various (pseudo)scalar-(pseudo)scalar, gauge boson-gauge boson and (pseudo) scalar-gauge boson interactions in $2 \to 2$ body processes. The unitarity of the S-matrix demands that the eigenvalues of it should be less than 8π [84,85]. In the FNSM, the unitary bounds are obtained from the S-matrix (using the equivalence theorem) as

$$\lambda_1(\Lambda) \leq 16\pi \quad \text{and} \quad |\lambda_1(\Lambda) + \lambda_2(\Lambda) \pm \sqrt{(\lambda_1(\Lambda) - \lambda_2(\Lambda))^2 + (2/3\lambda_3(\Lambda))^2}| \leq 16/3\pi. \tag{3.3}$$

We now use the relation in Eq. (2.11) to display theoretical bounds on the scalar singlet VEV v_s for various values of

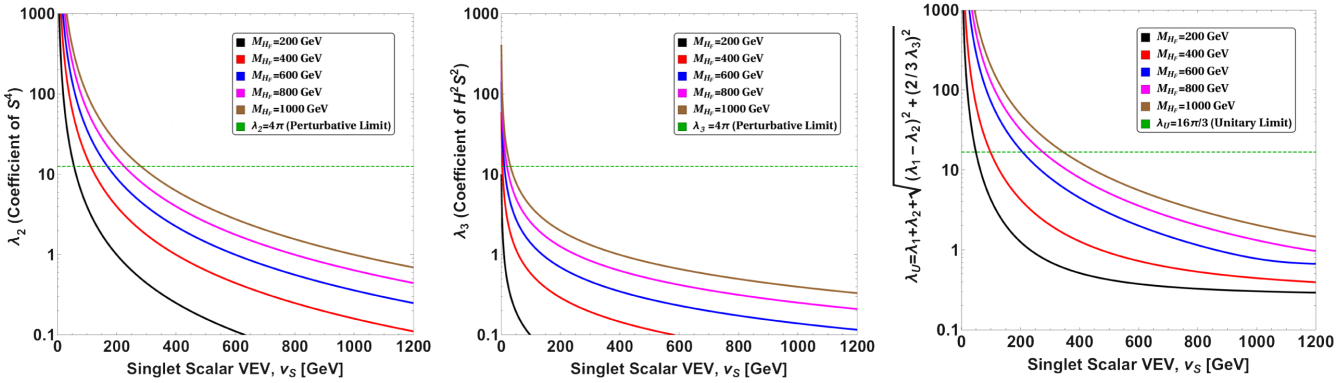

FIG. 2. In the first two plots we show the perturbative bounds on the quartic couplings $\lambda_{2,3}$ while the third plot shows the stringent unitary bounds on λ_U.

the heavy Higgs masses, M_{H_F} and M_{A_F}. In Fig. 2 we display the constraints on scalar quartic couplings coming from the perturbativity [Fig. 2 (left) and (middle)] and unitarity [Fig. 2 (right)] of the S-matrix. Here, we assume $M_{H_F} = M_{A_F}$ and $\cos\alpha = 0.995$, which agrees with the constraints from the Higgs boson coupling modifiers from the LHC measurements, which we will discuss in some detail later. Figure 2 (left) shows the $v_s - \lambda_2$ plane for $M_{H_F} =$ 200 GeV, 400 GeV, 600 GeV, 800 GeV, and 1000 GeV whereas in Fig. 2 (middle) the $v_s - \lambda_3$ plane is presented. The plane $v_s - \lambda_U (\equiv \lambda_1 + \lambda_2 + \sqrt{(\lambda_1 - \lambda_2)^2 + (2/3\lambda_3)^2})$ in Fig. 2 (right) shows the unitary bounds. We find that $|\lambda_U| \leq 16\pi/3$ is the most stringent upper bound for the scalar quartic couplings. From these plots, we can see that the lower limit on the scalar singlet VEV v_s is, for $M_{H_F} = (200, 400, 600, 800, 1000)$ GeV,
$v_s \geq (69, 138, 207, 276, 345)$ GeV. Note that we are working at the EW scale only, as detailed RGE analysis is beyond the scope of this work. We also choose the parameters in such a way that the scalar potential remains absolutely stable in all the directions of the scalar fields h, H_H, A_F. (Further details can be found in Ref. [84].)

C. Experimental constraints

To constrain the mixing angle α and the VEV of the FN singlet v_s, we use HL-LHC projections for the Higgs boson coupling modifiers κ_i at a CL of 2σ [86], as this machine configuration is the one with highest sensitivity among those we will consider in the analysis section. For a production cross section $\sigma(pp \to \phi)$ or a decay width $\phi \to X$ ($\phi = h, h^{\rm SM}$), we introduce,

$$\kappa_{pp}^2 = \frac{\sigma(pp \to h)}{\sigma(pp \to h^{\rm SM})}, \qquad \kappa_X^2 = \frac{\Gamma(h \to X)}{\Gamma(h^{\rm SM} \to X)}, \tag{3.4}$$

where $X = b\bar{b}, \tau^-\tau^+, W^-W^+, ZZ, \gamma\gamma$. Figure 3(a) shows all the regions complying with the aforementioned projections for each channel in the $\cos\alpha - v_s$ plane; here, the green,

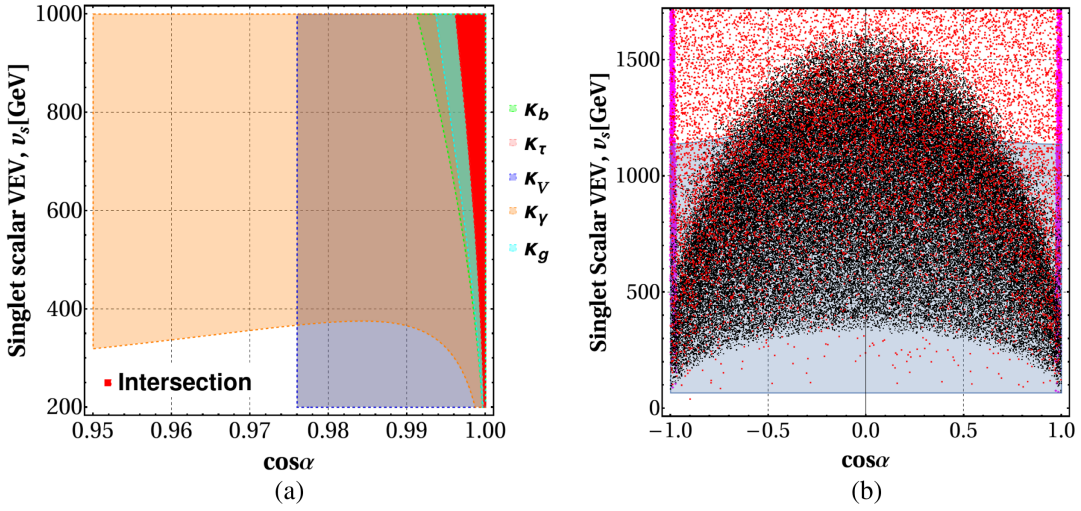

FIG. 3. VEV of the FN singlet v_s as a function of the cosine of the mixing angle α; constraints are from (a) the SM-like Higgs boson coupling modifiers and (b) flavor observables (as described in the text).

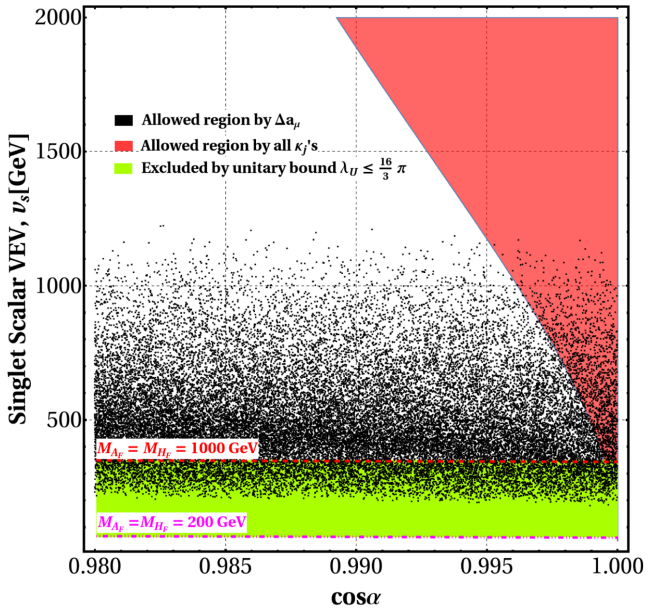

FIG. 4. VEV of the FN singlet v_s as a function of cosine of the mixing angle α in the presence of the most stringent ones among all theoretical and experimental constraints considered.

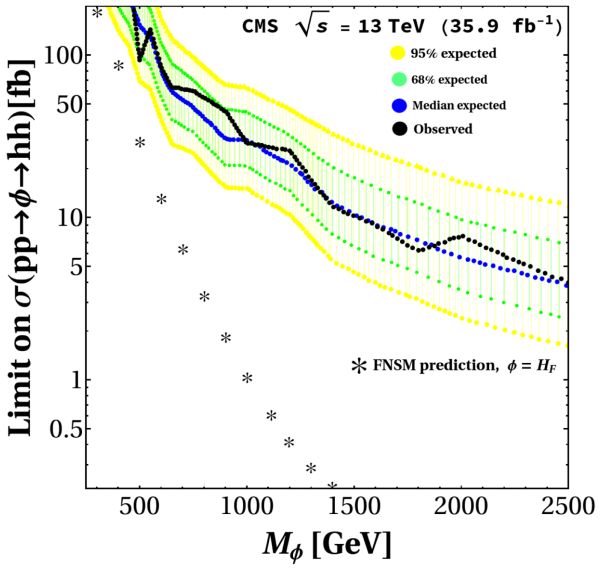

FIG. 5. Expected (blue points) and observed (black points) 95% CL exclusion limits on the production of a narrow, spin-0 resonance (ϕ) decaying into a pair of SM-like Higgs bosons at the LHC. The inner (green fill) and outer (yellow fill) bands indicate the regions containing 68% and 95% CL, respectively, results on the limit applicable to the $pp \to \phi \to hh$ cross section expected under the background-only hypothesis. The starred points are predictions in the FNSM for a selection of heavy Higgs masses ($\phi \equiv H_F$) containing BPs used in our analysis.

pink, blue, orange and cyan area corresponds to κ_b, κ_τ, κ_V, κ_γ, and κ_g, respectively, while the red area represents the intersection of all the areas allowed by all the individual channels. We consider $\tilde{Z}_{bb} = 0.01$ and $\tilde{Z}_{tt} = 0.4$ in the evaluations for the κ_X. Such values are well motivated because they simultaneously accommodate all the κ_X's. In fact, values in the $0.01 \leq \tilde{Z}_{bb} \leq 0.1$ and $0.1 \leq \tilde{Z}_{tt} \leq 1$ intervals have no important impact on the coupling modifiers, however, in the case when $\tilde{Z}_{bb} \geq 0.1$ and $\tilde{Z}_{tt} \geq 2$, a large reduction of allowed values in the $\cos\alpha - v_s$ plane is found [64,65].

Furthermore, we present in Fig. 3(b) the $\cos\alpha - v_s$ plane regions allowed by Δa_μ (black points), Δa_e (magenta points), $\mu \to 3e$ (red points) and $B_s^0 \to \mu^+\mu^-$ (blue area). We have also analyzed the decays $\tau \to 3\mu, \tau \to \mu\gamma, \mu \to e\gamma$, however, these processes are not very restrictive in the FNSM. This is mainly due to the choice we made for the matrix elements $\tilde{Z}_{\mu\mu}$ and $\tilde{Z}_{\tau\tau}$, as they play a subtle role in the couplings (see Table I) $\phi\mu^-\mu^+$ and $\phi\tau^-\tau^+$ ($\phi = h, H_F, A_F$), which have a significant impact on the observables $\tau \to 3\mu, \tau \to \mu\gamma, \mu \to e\gamma$. In fact, we use $\tilde{Z}_{\tau\tau} = 0.2$ and $\tilde{Z}_{\mu\mu} = 10^{-4}$ (hence, a strong hierarchy), otherwise the SM $h\mu^-\mu^+$ coupling would be swamped by new corrections due to the FNSM.[1] So the bounds coming from the processes $\tau \to 3\mu$, $\tau \to \mu\gamma$, $\mu \to e\gamma$ are not included in Fig. 3(b).

Then, in Fig. 4, we display the result of applying all discussed theoretical and experimental constraints, limitedly to the reduced interval $0.98 \leq \cos\alpha \leq 1$, since it is the region in which all the analyzed observables converge. Here, we only show the most restrictive bounds so as to not overload the plot. Among the latter, the unitarity bound plays a special role, as it helped us to find a lower limit for the singlet scalar VEV, v_s, depending on the flavon mass, e.g., for $M_{H_F} = 1000$ GeV one has $v_s \geq 345$ GeV. By comparison, the intersection of all κ_i's and Δa_μ imposes a less stringent upper limit of $v_s \leq 1200$ GeV.[2]

As far as the CP-even flavon mass M_{H_F} is concerned, to constrain it, we use the limit on the cross section of the process $pp \to \phi \to hh$ from [77], in which a combination of searches for SM-like Higgs boson pair production in proton-proton collisions at $\sqrt{s} = 13$ TeV and 35.9 fb^{-1} is reported. We present in Fig. 5 the cross section of the process $\sigma(pp \to H_F \to hh)$ in the FNSM as a function of M_{H_F} and its comparison with the limit on $\sigma(pp \to \Phi \to hh)$, where ϕ stands for a generic spin-0 resonance. Furthermore, we show in Figs. 6(a) and 6(b) a comparison between the FNSM predictions and the ATLAS

[1]Such a choice was adopted in the evaluation of $\kappa_{\tau\tau}$ and $\kappa_{\mu\mu}$, respectively, and then we scanned on the $\cos\alpha - v_s$ plane, as shown in Fig. 3(a).

[2]Notice that, to generate Figs. 3(a), 3(b), and 4, we have used our own *Mathematica* package, so-called `SpaceMath` [87], which is available upon request.

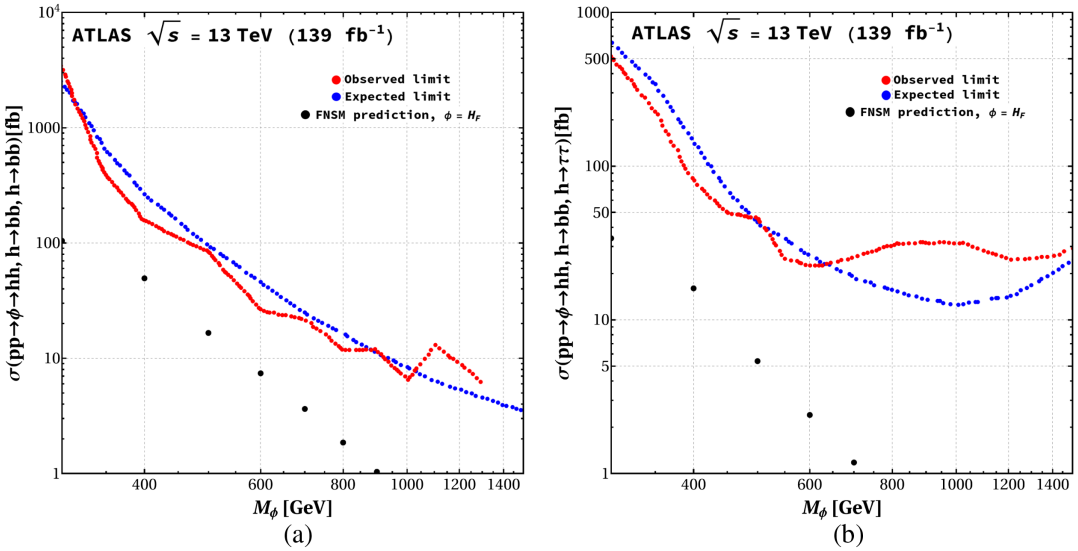

FIG. 6. Upper limits (observed and expected) on the cross section for di-Higgs production through an intermediate heavy particle ϕ as a function of the particle mass M_ϕ as obtained through the processes $pp \to H_F \to hh(h, \to b\bar{b}, h \to b\bar{b})$ (left) and $pp \to H_F \to hh$ $(h, \to b\bar{b}, h \to \tau^+\tau^-)$ (right).

Collaboration limits [88], now for individual channels with final states $b\bar{b}b\bar{b}$ and $b\bar{b}\tau^-\tau^+$, respectively. The most stringent constraints [89] come from $b\bar{b}\gamma\gamma$ production channel as shown in Fig. 7. In obtaining such limits, we have evaluated the inclusive cross section of our signal process, wherein we have used $v_s = 1000$ GeV and $\cos\alpha = 0.995$. It is observed that the $M_{H_F} =$ 300–1000 GeV interval satisfies the bounds imposed, so we will define benchmark points (BPs) with H_F masses herein. The model parameter space in this analysis is also consistent from the other search channels $pp \to H_F \to ZZ$ at ATLAS [13] and $pp \to H_F \to WW$ at CMS [90].

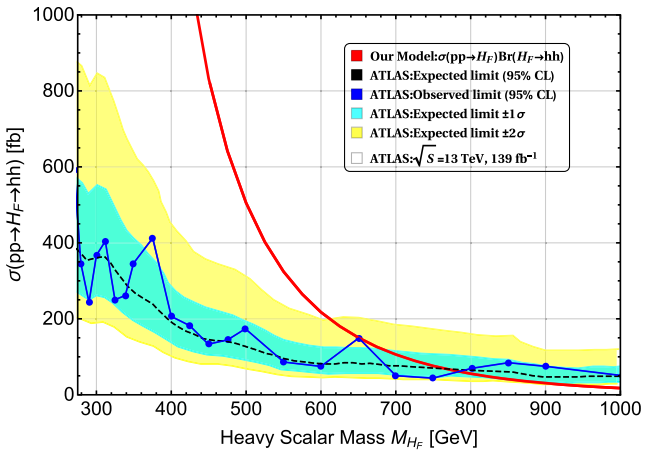

FIG. 7. Upper limits (observed and expected) on the cross section for di-Higgs production [89] through an intermediate heavy particle ϕ as a function of the particle mass M_ϕ as obtained through the process $pp \to H_F \to hh(h, \to b\bar{b}, h \to \gamma\gamma)$.

D. Constraints on $\tilde{Z}_{tc}$ from flavor-violating Higgs decays

Finally, because the $g_{H_F tc}$ coupling is proportional to the $\tilde{Z}_{tc}$ matrix element, we need a bound on it in order to evaluate the $H_F \to tc$ decay. Currently, there no specific processes that provide a stringent limit $\tilde{Z}_{tc}$, but we can estimate its order of magnitude by considering the upper limit on the branching ratio (BR) of $t \to ch$ at $< 1.1 \times 10^{-3}$ [91]. We also consider the prospects for $\mathrm{BR}(t \to ch) < 4.3 \times 10^{-5}$ searches at the FCC-hh [92]. The resulting

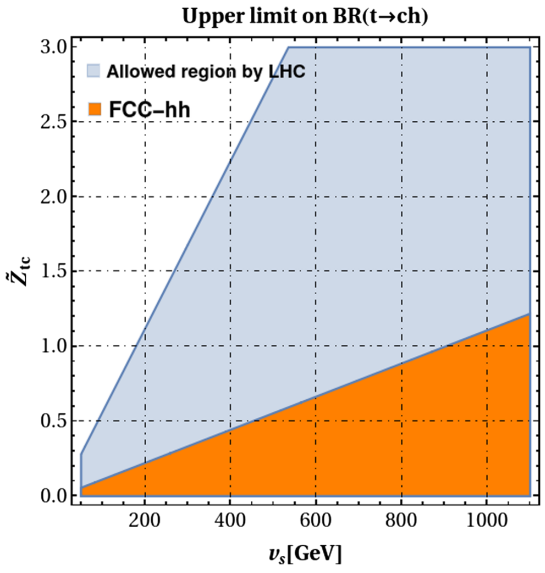

FIG. 8. Allowed region in the v_s-$\tilde{Z}_{tc}$ plane from the current bound on $\mathrm{BR}(t \to ch) < 1.1 \times 10^{-3}$ (blue color) and the projection at the FCC-hh (orange color).

allowed region in the $v_s - \tilde{Z}_{tc}$ plane is illustrated in Fig. 8. It is worth noting here that the behavior of the $\tilde{Z}_{tc}$ matrix element shows an increasing (decreasing) trend as v_s increases (decreases). This observation is expected since the g_{htc} coupling is governed by $\tilde{Z}_{tc}/v_s$. In order to have a realistic evaluation of the observables studied here, we adopt conservative values for $\tilde{Z}_{tc}$ and v_s.

IV. COLLIDER ANALYSIS

Following our discussions on various model parameters and their constraints, we now study the collider signature emerging in the FNSM in the form of a singletlike CP-even heavy Higgs scalar H_F decaying into SM-like Higgs h, neutral gauge bosons Z and top-charm quark pairs at Run 3 of the LHC as well as the HL-LHC, assuming $\sqrt{s} =$ 14 TeV for both and a luminosity of 3000 fb^{-1}. In our analysis, we adopt $c_\alpha = 0.995$ (i.e., a small mixing angle α between the CP-even part of the doublet and singlet scalar fields) and assume for the cutoff scale $\Lambda_F = 10$ TeV, in order to easily avoid theoretical as well as experimental bounds (as discussed in the previous section).

Specifically, at the LHC, we consider the resonant production of the H_F state via gluon-gluon fusion, followed by its decay into two on-shell SM-like Higgs bosons (h), neutral gauge bosons Z and a top-charm quark pair. For hh production, one of the Higgs h decays into a pair of b-tagged jets while the other decays into two photons, i.e., $pp \to H_F \to hh(h \to b\bar{b}, h \to \gamma\gamma)$: recall Fig. 1. For the ZZ channel, a Z decays into a SFOS pair; while for tc channel, the top quark decays into $\ell\nu_\ell b$, with $\ell = e^-, e^+, \mu^-, \mu^+$. Hence, we have three separate final states. The first one has two photons (γ) and two b-jets, the second one has four leptons, and the third one contains a charged lepton plus its corresponding neutrino and two jets (one of them is a b-jet and the other is a c-jet). They all have some amount of hadronic activity generated from the initial state. Here, we only analyze the channels $H_F \to hh, ZZ, tc$, since it is to be noted that the $A_F hh$ and $A_F ZZ$ couplings are zero because of CP conservation, hence the twin production processes $pp \to A_F \to hh, ZZ$ via gluon-gluon fusion is not possible. The $A_F \to tc$ decay is dedicated for future analysis.

We use FeynRules [93] to built the FNSM model and produce the UFO files for MadGraph-2.6.5 [94]. Using the ensuing particle spectrum into MadGraph-2.6.5, we calculate the production cross section of the aforementioned production and decay process. The MadGraph_aMC@NLO [94] framework has been used to generate the background events in the SM. Subsequent showering and hadronization have been performed with PYTHIA-8 [95]. The detector response has been emulated using DELPHES-3.1.2 [96]. The default ATLAS configuration card which comes along with the DELPHES-3.4.2 package has been used in the entirety of this analysis. For both the signal and background processes, we consider the leading order (LO) cross sections computed by MadGraph_aMC@NLO, unless stated otherwise.

In the previous processes, we focus on the complete FN diagonal basis, meaning no heavy Higgs flavor-violating decay is present. This choice allow us to explore the large BRs to other channels, which could potentially provide a large signal significance in our study. We discuss the details now. Afterwards, we consider the FN off-diagonal basis to have new signals. This modification enables us to investigate the effects of heavy Higgs flavor-violating interactions, which can have significant implications for our understanding of the FN-Higgs sector.

We first generate the signal events for various heavy CP-even flavon masses, $M_{H_F} (= M_{A_F})$ considering $\tilde{Z}_{ij} = 0 (i \neq j)$. The latter have been varied from 260 to 1000 GeV with a step size of 10 GeV. We then take $v_s = 1000$ GeV; such a large VEV produces a small production cross section

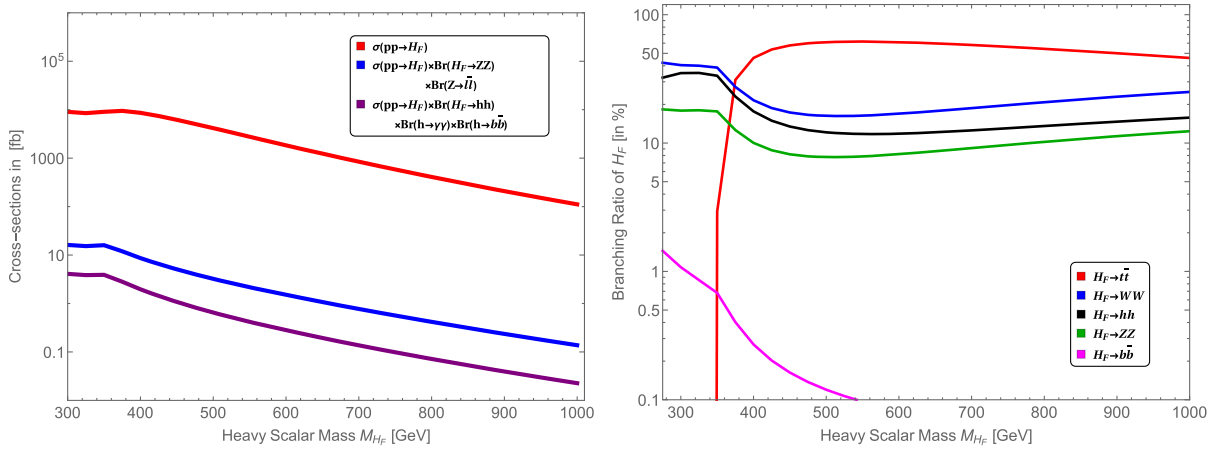

FIG. 9. The red (blue and purple) line on the left plot stands for the cross section of the processes $pp \to H_F$ ($pp \to H_F \to hh(h \to \gamma\gamma, h \to b\bar{b})$ and $pp \to H_F \to ZZ(Z \to \ell\bar{\ell})$) at 14 TeV. The variation in the BRs of the heavy CP-even flavon mass M_{H_F} is displayed in the right plot. The heavy Higgs flavor-violating decay is absent here, i.e., $\tilde{Z}_{ij} = 0 (i \neq j)$.

TABLE II. The input parameters of the three BPs (BP1, BP2, and BP3) used in the remainder of the paper. We have $M_h = 125.5$ GeV, $\cos\alpha = 0.995$, $v_s = 1000$ GeV, and $\Lambda_F = 1$ TeV is this kept fixed for all BPs.

BPs (GeV)	The other input parameters
BP1 ($M_{H_F} = 800$)	$M_{A_F} = 800$ GeV, $\lambda_1 = 0.36$, $\lambda_2 = 0.64$, $\lambda_3 = 0.25$
BP2 ($M_{H_F} = 900$)	$M_{A_F} = 900$ GeV, $\lambda_1 = 0.39$, $\lambda_2 = 0.81$, $\lambda_3 = 0.32$
BP3 ($M_{H_F} = 1000$)	$M_{A_F} = 1000$ GeV, $\lambda_1 = 0.42$, $\lambda_2 = 0.99$, $\lambda_3 = 0.40$

$\sigma(pp \to H_F)$ and a correspondingly small partial width $\Gamma(H_F \to hh, ZZ)$, hence small (but non-negligible, for our purposes) signal rates, however, this is necessary to comply with all theoretical and experimental limits. We display the cross section of the process $pp \to H_F$, $pp \to H_F \to hh(h \to \gamma\gamma, h \to b\bar{b})$ and $pp \to H_F \to ZZ(Z \to \ell\bar{\ell})$ on the left-hand side of Fig. 9, where the red line stands for $\sigma(pp \to H_F)$.

One can thus understand the nature of the production and decay rates as follows. The production cross sections of the heavy CP-even flavon H_F (or pseudoscalar A_F, for that matter) mainly depends on the $g_{H_F t\bar{t}} = \frac{c_\alpha v + s_\alpha v_s}{v_s}\frac{y_t}{\sqrt{2}}$ ($g_{A_F t\bar{t}} = \frac{v}{v_s}\frac{y_t}{\sqrt{2}}$) coupling, as the latter goes into the effective Higgs-to-two gluon vertex, hgg. The corresponding term in the Lagrangian is given by [97]

$$\mathcal{L}_{\text{eff}} = \frac{1}{v} g_{hgg} h G_{\mu\nu} G^{\mu\nu}, \tag{4.1}$$

$$g_{Sgg} = -i\frac{\alpha_S}{8\pi}\tau(1 + (1-\tau)f(\tau)) \quad \text{with} \quad \tau = \frac{4M_t^2}{M_h^2}, \tag{4.2}$$

$$f(\tau) = \begin{cases} \left(\sin^{-1}\sqrt{\frac{1}{\tau}}\right)^2, & \tau \geq 1, \\ -\frac{1}{4}\left[\ln\frac{1+\sqrt{1-\tau}}{1-\sqrt{1-\tau}} - i\pi\right]^2 & \tau < 1. \end{cases} \tag{4.3}$$

In this model, the ggh, ggH_F, and ggA_F couplings take the following form: $g_{hgg} = (\frac{c_\alpha v_s - s_\alpha v}{v_s})g_{Sgg}$, $g_{H_F gg} = (\frac{c_\alpha v + s_\alpha v_s}{v_s})g_{Sgg}$, and $g_{A_F gg} = \frac{v}{v_s}(-i\alpha_S/\pi)\tau f(\tau)$,[3] respectively. It is to be noted that, for $M_{H_F, A_F} > 2M_t$, $f(\tau) = -\frac{1}{4}\left[\ln\frac{1+\sqrt{1-\tau}}{1-\sqrt{1-\tau}} - i\pi\right]^2$. Hence, one can understand the shape of the plot by exploiting these functions. The BRs of H_F into various channels for $v_s = 1000$ GeV are shown on the right-hand side of Fig. 9. From the BR plot, we can see that, for heavier H_F masses, this state dominantly decays into $t\bar{t}$. For small masses, $H_F \to WW$ dominates. Yet, $H_F \to hh$ is the third, while $H_F \to ZZ$ is the fourth largest decay channels. In the next subsections, we will focus on discussing the processes $H_F \to hh(h \to b\bar{b}, h \to \gamma\gamma)$ and $H_F \to ZZ(Z \to \ell\bar{\ell})$ for the diagonal and $H_F \to tc(t \to b\ell\nu_\ell)$ for off-diagonal scenario, respectively. These processes are of particular interest because they are not as strongly suppressed by standard model backgrounds compared to the $H_F \to t\bar{t}$ and $H_F \to WW$ decays.

A. $pp \to H_F \to hh(h \to \gamma\gamma, h \to b\bar{b})$

The major SM backgrounds typically have the form $hh + X$ (where X is known SM particles), which includes SM-Higgs pair hh production, $h + X$ like hZ, $hb\bar{b}$, and $ht\bar{t}$, as well as the non-Higgs processes which include $t\bar{t}$ and $t\bar{t}\gamma$ (here, leptons may fake as photons) as well as $b\bar{b}\gamma\gamma$, $c\bar{c}\gamma\gamma$ and $jj\gamma\gamma$ (where c-jets and light-jets may fake b-jets). The other relevant reducible backgrounds comprise $b\bar{b}j\gamma$, $c\bar{c}j\gamma$, and $b\bar{b}jj$, where c-jets may appear as b-jets and a light-jet may fake a photon. The fake rate of a light-jet j into a photon depends on the momentum of the jet, p_T^j [100], as $9.3 \times 10^{-3}\exp(-p_T^j/27.5\text{ GeV})$. The c-jet is misidentified as a b-jet with a rate of 3.5% whereas a light-jet mimics a b-jet with a rate of 0.135% [101].

We next present a detailed discussion of the collider search strategy employed to maximize the signal significance in the search channel $pp \to H_F \to hh(h \to \gamma\gamma, h \to b\bar{b})$. To start with, though, we show the production and decay cross section $pp \to H_F \to hh(h \to \gamma\gamma, h \to b\bar{b})$ for the three BPs presented in Table II (with, in particular, $M_{H_F} = 800$ GeV, 900 GeV, and 1000 GeV, as seen in Table III). The corresponding dominant SM backgrounds are shown in Table IV.

Any charged objects (leptons or jets) or photons produced in any hard scattering process at the LHC will be observed in the detector if and only if they satisfy certain geometric criteria, known as acceptance cuts. These are the same for both the signal and background events and reproduce the accessible region of the detector. We will then have to ask that both signal and background events pass these acceptance cuts, which are, in general, not sufficient to separate the two samples. However, eventually, we will construct various kinematic observables and study their distributions. Next, we will decide the final selection cuts after studying the distinguishing features of those distributions between signal and backgrounds, so as to increase the former and decrease the latter. We base this approach on a Monte Carlo (MC) analysis using the tools previously described.

In our current scenario, an event is required to have exactly two b-tagged jets and two isolated photons (γ) in

[3] A_F is CP-odd scalar and h, H_F is CP-even scalar so, once the couplings with left and right fields are written in terms of Dirac fields, the Hermitian part of the coupling in Eq. (2.12) gives rise to an $i = \sqrt{-1}$ coupling for h, H_F, and a γ_5 coupling for A_F. So the result of the top-quark loop integral is different for h, H_F, and A_F [98,99].

TABLE III. The BR($H_F \to hh$) and cross sections for the processes $pp \to H_F$ and $\sigma(pp \to H_F \to hh, h \to \gamma\gamma, h \to b\bar{b})$ for three BPs (BP1, BP2, and BP3) used in the remainder of the paper.

	BRs and cross sections (pb)		
BPs (GeV)	BR($H_F \to hh$)	$\sigma(pp \to H_F)$	$\sigma(pp \to H_F \to hh, h \to \gamma\gamma, h \to b\bar{b})$
BP1 ($M_{H_F} = 800$)	0.14	0.41	7.18×10^{-5}
BP2 ($M_{H_F} = 900$)	0.15	0.21	3.95×10^{-5}
BP3 ($M_{H_F} = 1000$)	0.16	0.11	2.27×10^{-5}

TABLE IV. The cross sections for the most relevant SM background processes. (Note that these background rates will be multiplied by the fake rates during the analysis.)

SM backgrounds	Cross section (pb)
$pp \to b\bar{b}\gamma\gamma$	4.57
$pp \to Zh\,(Z \to b\bar{b}, h \to \gamma\gamma)$	1.40×10^{-4}
$pp \to b\bar{b}j\gamma$	7470.02
$pp \to b\bar{b}jj$ (j mimic as photon)	5.03×10^{6}
$pp \to c\bar{c}\gamma\gamma$	6.21
$pp \to c\bar{c}j\gamma$ (c appear as b-tagged jets, j mimic as photon)	2085.01
$pp \to jj\gamma\gamma$ (j appear as b-tagged jets)	65.23
$pp \to t\bar{t}(t \to \overline{\ell}\nu_\ell b, \bar{t} \to \ell\bar{\nu}_\ell\bar{b})$	6.17×10^{-5}
$pp \to t\bar{t}(t \to jjb, \bar{t} \to jj\bar{b})$ (ℓ, j mimic as photon)	202.15

the final state. However, we do not put any constraints on the number of light-jets. We then adopt the following acceptance cuts:

(i) $p_T^{\gamma} > 20$ GeV;

(ii) $p_T^{e/\mu} > 20$ GeV (if an electron/muon is present, for b-tagging purposes);

(iii) $p_T^{j} > 40$ GeV, where j stands for light-jets as well as b-jets;

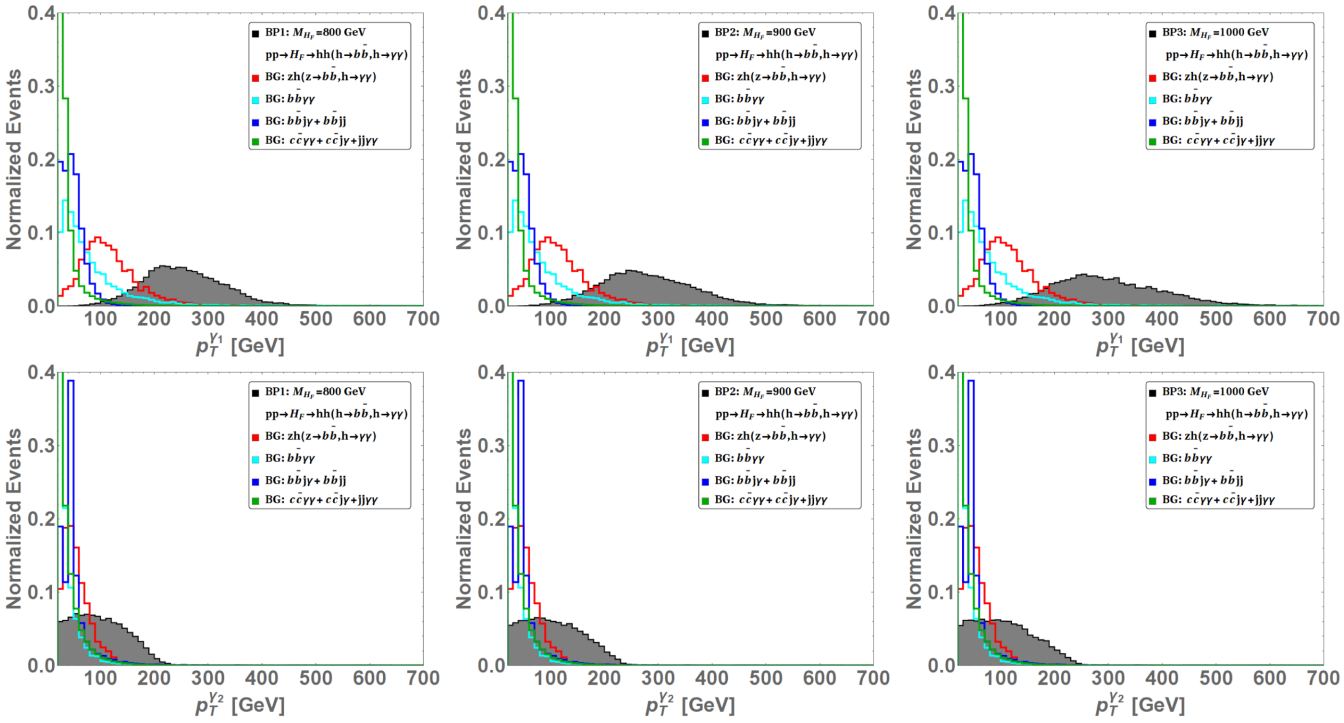

FIG. 10. Normalized distributions in photon transverse momentum for signal and total background after the acceptance cuts.

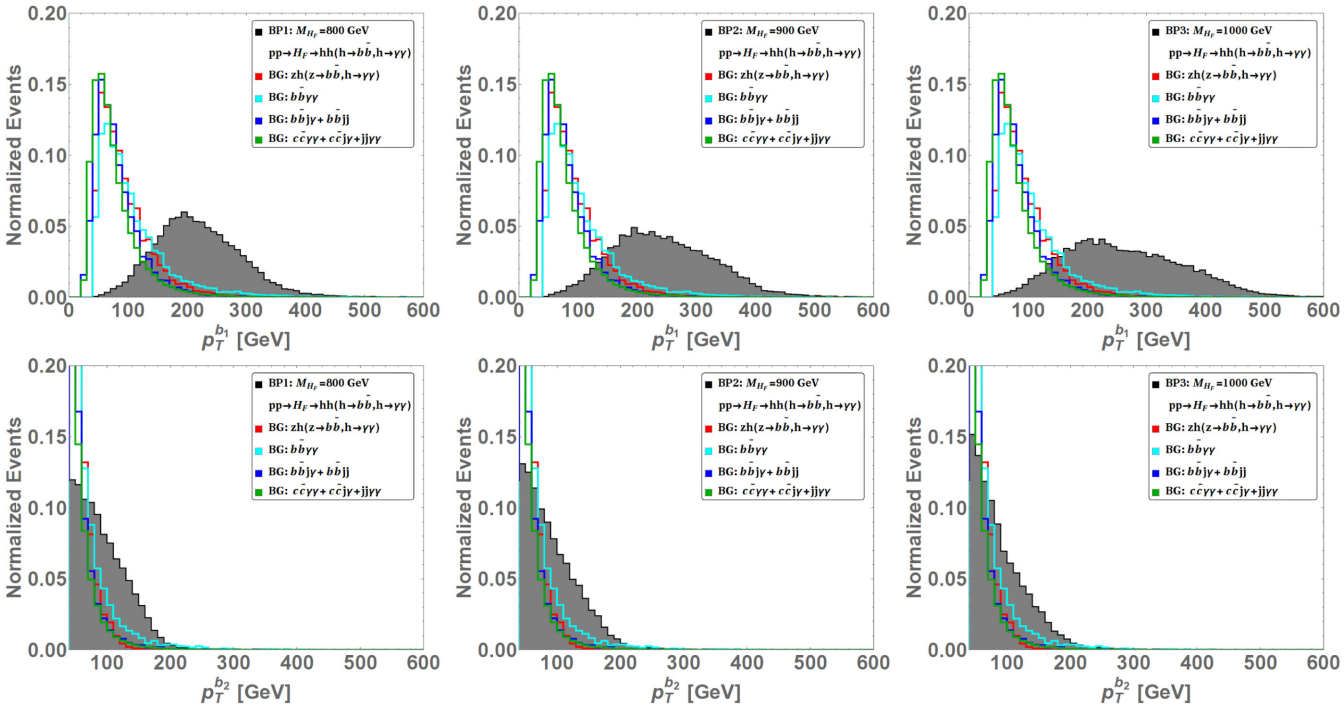

FIG. 11. Normalized distributions in b-jet transverse momentum for signal and total background after the acceptance cuts.

(iv) $|\eta_\ell| \leq 2.5$ (again, $\ell = e/\mu$), $|\eta_\gamma| \leq 2.0$ and $|\eta_j| \leq 2.0$. After considering these basic requirements, we apply a stronger selection (using additional kinematic variables) in order to enhance the signal-to-background ratio, as explained. A variety of such observables have been used to design the optimized signal region (SR), i.e., where the significance is maximized. First and foremost, the transverse momentum of photons ($p_T^{\gamma_1}$, $p_T^{\gamma_2}$) and b-jets

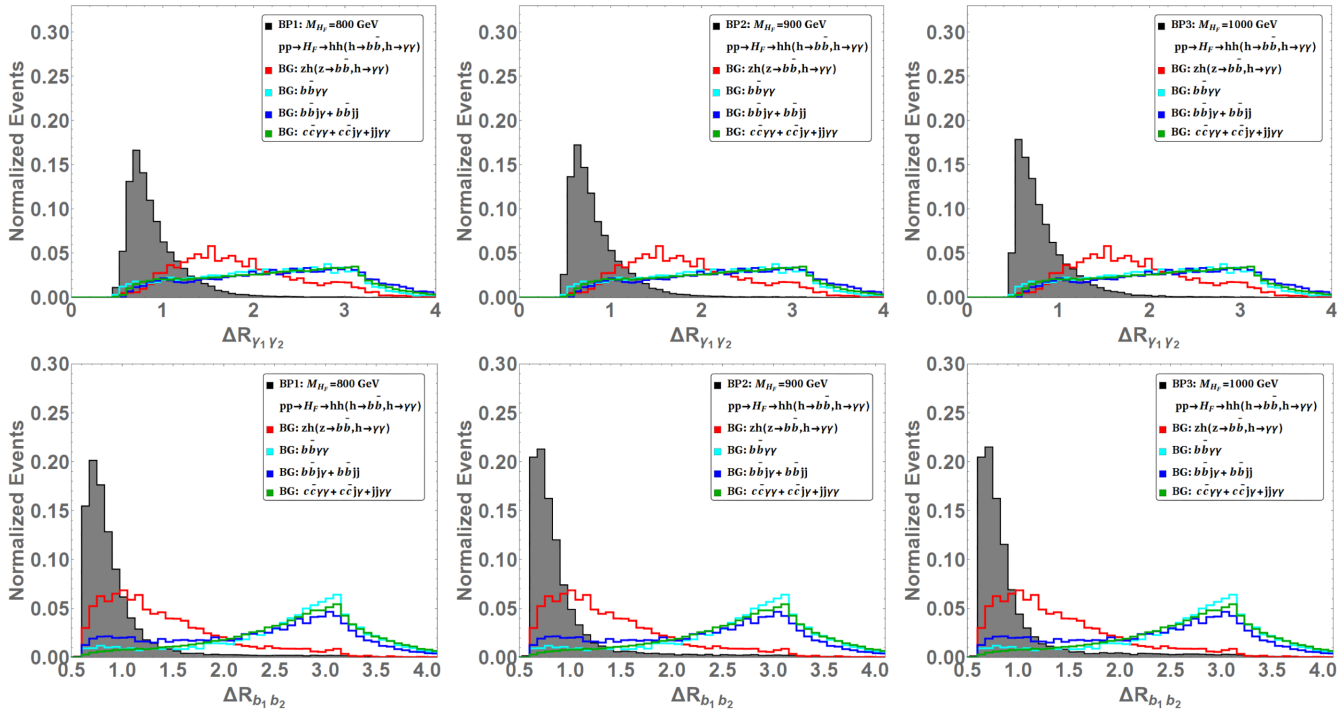

FIG. 12. Normalized distributions in diphoton and dijet separation for signal and total background after the acceptance cuts.

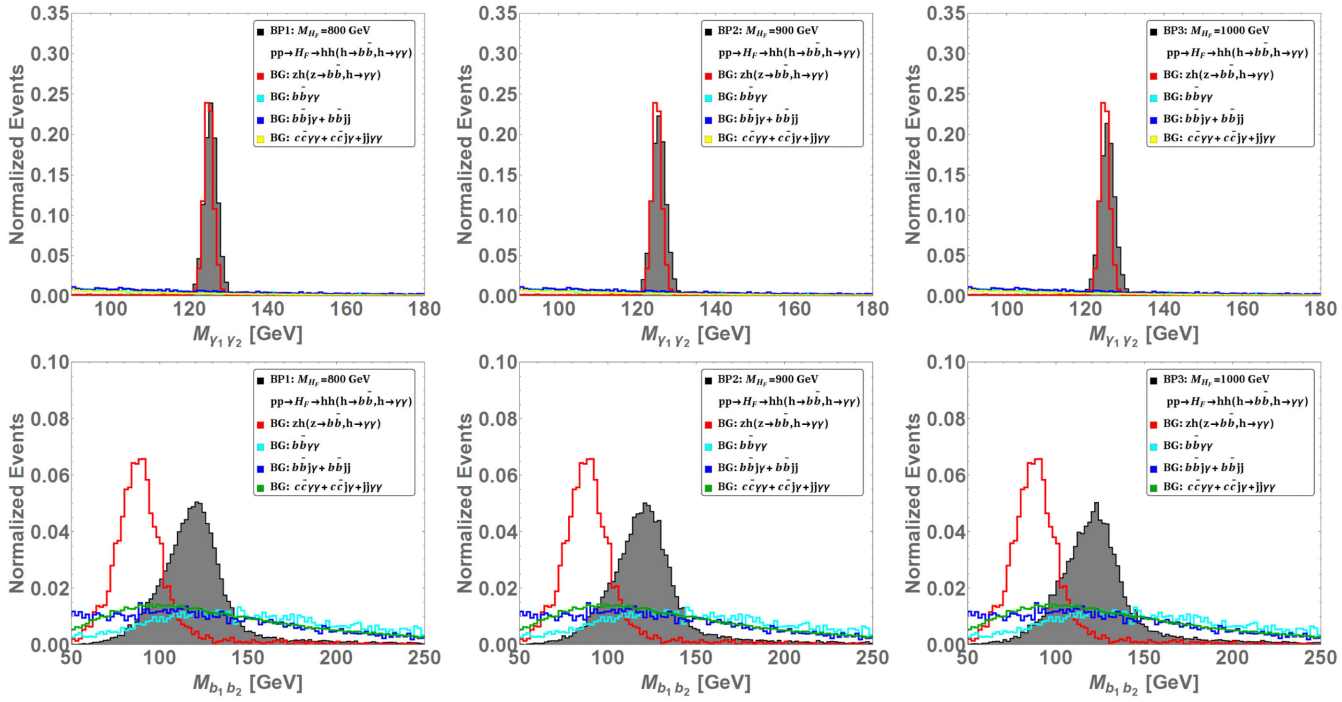

FIG. 13. Normalized distributions in diphoton and dijet invariant mass for signal and total background after the acceptance cuts.

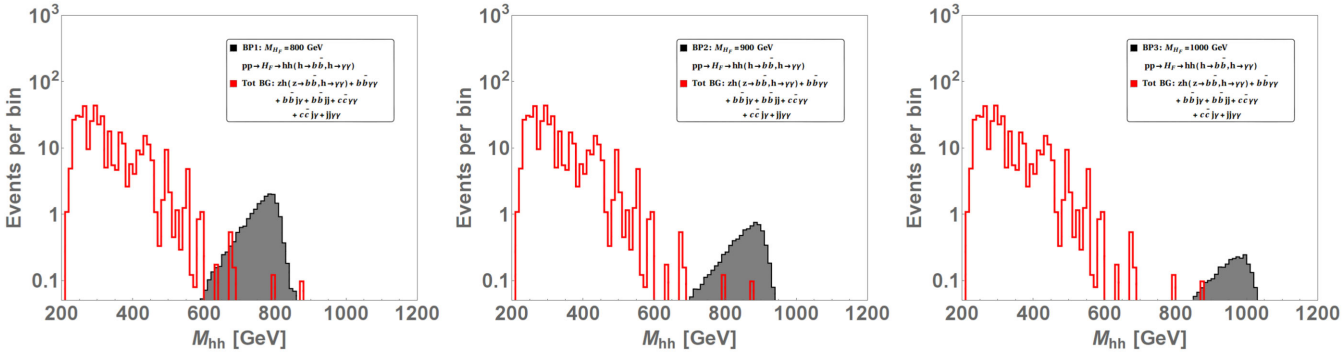

FIG. 14. Distributions in the final-state invariant mass for signal and total background after the acceptance cuts as well as the selection ones on $p_T^{\gamma_{1,2}}$, $p_T^{b_{1,2}}$, $M_{\gamma_1\gamma_2}$, $M_{b_1 b_2}$, $\Delta R_{\gamma_1\gamma_2}$, and $\Delta R_{b_1 b_2}$, as shown in Table V.

$(p_T^{b_1}, p_T^{b_2})$[4] will be studied. In addition, the separation between the two final-state photons $\Delta R_{\gamma_1\gamma_2}$ and b-jets $\Delta R_{b_1 b_2}$ are also used. The separation between two detector objects, ΔR, is defined as $\Delta R = \sqrt{\Delta\eta^2 + \Delta\phi^2}$, where $\Delta\eta$ and $\Delta\phi$ are the differences in pseudorapidity and azimuthal angle, respectively. Then, the invariant mass of the final state photons ($M_{\gamma_1\gamma_2}$) and b-jets ($M_{b_1 b_2}$) will also be used to discriminate between signal and backgrounds, where we have introduced $M_{ab} = \sqrt{(E^a + E^b)^2 - \sum_{i=x,y,x}(p_i^a + p_i^b)^2}$, with $ab = \gamma_1\gamma_2$ or

[4]Here, 1 and 2 represents the p_T ordered leading and subleading photon and b-jet in the final state.

TABLE V. The optimized SR as a function of the H_F mass.

	Kinematic variables and cuts	
	Observable	Value
SR	$p_T^{\gamma_{1,2}}$	>35.0 (GeV)
	$p_T^{b_{1,2}}$	>40.0 (GeV)
	$M_{\gamma_1\gamma_2}$	122.5–128.5 (GeV)
	$M_{b_1 b_2}$	70.0–135.0 (GeV)
	$\Delta R_{\gamma_1\gamma_2}$	0.4–4.6
	$\Delta R_{b_1 b_2}$	0.4–3.6
	M_{hh} (varied with M_{H_F})	$0.7M_{H_F} - 1.1M_{H_F}$

TABLE VI. The signal significance $\sigma = \frac{S}{\sqrt{S+B}}$ for BP1, BP2, and BP3 corresponding to the optimized SR are shown. In addition, the total background yield and the total signal yield are also given at $\sqrt{s} = 14$ TeV with integrated luminosity $\mathcal{L} = 3000$ fb^{-1}.

Benchmark points: Signal and significances								
BP1 ($M_{H_F} = 800$ GeV)			BP2 ($M_{H_F} = 900$ GeV)			BP3 ($M_{H_F} = 1000$ GeV)		
Number of signal	Number of background	Significance	Number of signal	Number of background	Significance	Number of signal	Number of background	Significance
18.45	5.65	3.81	7.92	3.72	2.32	3.10	~3	1.25

$b_1 b_2$. Finally, we use the invariant mass M_{hh} for the final extraction. The M_{hh} variable has been calculated as $M_{hh} = \sqrt{(E^{\gamma_1}+E^{\gamma_2}+E^{b_1}+E^{b_2})^2 - \sum_{i=x,y,z}(p_i^{\gamma_1}+p_i^{\gamma_2}+p_i^{b_1}+p_i^{b_2})^2}$. In the above formulas, E and $p_i (i = x, y, z)$ stand for the energy and three-momentum component of the final state particles, respectively.

The (arbitrarily) normalized distributions of all these kinematic variables for the three signal BPs and the total background are shown in Figs. 10–14. Based on their inspection, as intimated, we then perform a detailed cut-based analysis to maximize the signal significance against the background. The sequence of constraints adopted is shown in Table V. Specifically, notice that, in applying the last requirement herein (on the M_{hh} variable), one may assume that the M_{H_F} value is a trial one, if it were not already known from previous analysis.

The signal yields for BP1, BP2, and BP3, along with the corresponding background ones, obtained after the application of the acceptance and selection cuts defining the SR, are shown in Table VI for $\sqrt{s} = 14$ TeV and, e.g., $\mathcal{L} = 3000$ fb^{-1}. We initially calculate the signal significance using the relation $\sigma = \frac{S}{\sqrt{S+B}}$. Here, S and B stand for the signal and (total SM) background rates, respectively. The number of S and B events is obtained as $S, B = \epsilon A \sigma_{S,B} \mathcal{L}$, where ϵ and A stand for the selection and acceptance cut efficiency, respectively, $\sigma_{S,B}$ is the S or B cross section and $\mathcal{L}$ is the luminosity. Based on these definitions, it is clear from Table VI that strong HL-LHC sensitivity exists for all M_{H_F} choices, ranging from discovery (at small masses) to exclusion (at high masses). (It should be appreciated that these significances would be reduced by as much as 30% in the absence of the final M_{hh} selection.) In fact, one can also consider the systematic uncertainty in various SM background estimations while calculating the final signal significance as[5] $\sigma = \frac{S}{\sqrt{S+B+(\kappa B)^2}}$, where κ is the percentage of systematic uncertainty [102]. Upon adding 5% for the latter, the significance in Table VI for BP1 decreases to 3.75 while for BP2 and BP3 it becomes 2.31 and 1.24, respectively. Hence, the HL-LHC sensitivity is very stable against unknowns affecting the data sample estimations, whatever the origin.

We now derive the various projected limits over the $M_{H_F} - v_s$ plane. It is to be noted that the variation of the singlet scalar VEV v_s will directly change the $H_F hh$ coupling and correspondingly the production cross section $\sigma(pp \to H_F \to hh)$. In particular, the smaller the former the larger the latter. To accurately delineate sensitivity regions, we generate a large number of signal events for various combinations of heavy CP-even flavon mass, M_{H_F}, and singlet scalar VEV, v_s. Specifically, $M_{H_F} (\equiv M_{A_F})$ has been varied from 800 GeV to 1000 GeV with a step size of 5 GeV while v_s has been varied between 500 GeV and 1000 GeV with a step size of 25 GeV. The projected exclusion (2σ) region derived from the $\gamma\gamma b\bar{b}$ final state in the $M_{H_F} - v_s$ plane are given in Fig. 15. The left plot is drawn for $\mathcal{L} = 3000$ fb^{-1} (HL-LHC). Again, the left plot in Fig. 15 is shown with no systematic uncertainty, i.e., $\kappa = 0$, while the right plot is drawn based on a systematic uncertainty $\kappa = 5\%$. From the right plot, we should mention that the limits drop somewhat (by 5–10%) upon introducing a systematic uncertainty of $\kappa = 5\%$, hence not too drastic a reduction of sensitivity in general (as already remarked for our BPs).

B. $pp \to H_F \to ZZ(Z \to \ell\bar{\ell})$

In this section, we now discuss the signatures involving the final state with four leptons ($2\bar{\ell} + 2\ell$) in the context of HL-LHC. The primary contribution to these signatures typically arises from the process $pp \to H_F \to ZZ$, where each Z boson further decays into a lepton-antilepton pair ($Z \to \ell\bar{\ell}$). To investigate the leptons' final state signatures, we have selected the same three benchmark points, which are $M_{H_F} = 800$ GeV, 900 GeV, and 1000 GeV, respectively. The Table VII displays the signal cross sections for different processes. Among them, the primary background in the Standard Model is the production of two Z bosons accompanied by jets ($ZZ +$ jets). In addition, there are other significant reducible backgrounds, such as the production of top quark pairs with jets ($t\bar{t} +$ jets), the production of a Z boson and a Higgs boson with jets

[5]To include the systematic uncertainty in $\sigma = \frac{S}{\sqrt{S+B}}$, one can replace $S + B$ in the denominator by the quadratic sum of $\sqrt{S+B}$ and use $\sigma_b = \kappa B$ [102], i.e., $\sigma = \frac{S}{\sqrt{S+B+(\kappa B)^2}}$, with κ being the percentage of systematic uncertainty of the total background.

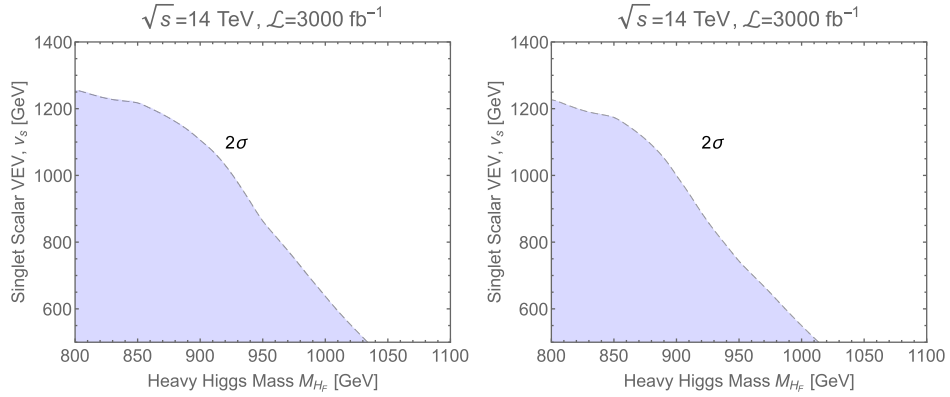

FIG. 15. The projected exclusion (light blue) and discovery (dark blue) regions in the $M_{H_F} - v_s$ plane. These plots are drawn for $\mathcal{L} = 3000$ fb^{-1}. The right plot is drawn considering a systematic uncertainty $\kappa = 5\%$.

($Zh +$ jets), and so on. We have included all the relevant Standard Model backgrounds in the Table VIII.

In this particular scenario, the event must contain precisely four isolated leptons, consisting of two positively charged leptons and two negatively charged leptons. This requirement ensures the presence of same-flavor opposite-sign (SFOS) leptons (electron and/or muon) in the final state. However, no specific constraints are imposed on the number of light jets present in the event. We then adopt the following acceptance cuts:

(i) $p_T^{\gamma} > 20$ GeV;
(ii) $p_T^{e/\mu} > 20$ GeV;
(iii) $p_T^{j} > 40$ GeV, where j stands for light-jets as well as b-jets;
(iv) $|\eta_\ell| \leq 2.5$ (again, $\ell = e/\mu$), $|\eta_\gamma| \leq 2.0$ and $|\eta_j| \leq 2.0$.

After considering these basic requirements, we apply additional cuts using kinematic variables to enhance the signal-to-background ratio. Various such kinematic variables have been used to design the optimized signal region (SR), i.e., where the significance is maximized. First and foremost, the transverse momentum of the leptons ($p_T^{\ell_i}$, $i = 1..4$) and the minimum invariant mass $M_{\ell\ell}^{\min}$ out of four combinations ($M_{\ell_i\ell_j}, i, j = 1..4$) and total transverse momentum of four leptons ($\sum p_T^{\ell_i}$) will be studied.

Finally, we use the invariant mass M_{ZZ} for the final extraction. The M_{ZZ} variable has been calculated as $M_{ZZ} = \sqrt{(E^{\ell_1}+E^{\ell_2}+E^{\ell_3}+E^{\ell_4})^2 - \sum_{i=x,y,z}(p_i^{\ell_1}+p_i^{\ell_2}+p_i^{\ell_3}+p_i^{\ell_4})^2}$. Here E and $p_i (i = x, y, z)$ stand for the energy and three-momentum component of the final state leptons, respectively.

The normalized distributions of all these kinematic variables for the three signal benchmark points (BPs) and the total background for this analysis are shown in Figs. 16–17. We then perform a detailed cut-based analysis to maximize the signal significance against the SM backgrounds. The figures labeled 16 and 17 illustrate the normalized distributions of various kinematic variables for the three signal benchmark points as well as the total background in this analysis. Subsequently, we employ a thorough cut-based analysis technique to optimize the signal significance with respect to the Standard Model backgrounds. The specific sequence of cuts applied during this analysis is presented in Table IX.

The Table X shows the signal yields for three benchmark points and the corresponding yields for the SM background. We obtained these numbers after applying acceptance and selection cuts that define the signal region (SR).

TABLE VII. The BR($H_F \to ZZ$) and cross sections for the processes $pp \to H_F$ and $\sigma(pp \to H_F \to ZZ, Z \to \ell\bar{\ell})$ for three BPs (BP1, BP2, and BP3) used in the remainder of the paper.

	BRs and cross sections (pb)		
BPs (GeV)	BR($H_F \to ZZ$)	$\sigma(pp \to H_F)$	$\sigma(pp \to H_F \to ZZ, Z \to \ell\bar{\ell})$
BP1 ($M_{H_F} = 800$)	0.10	0.41	1.90×10^{-5}
BP2 ($M_{H_F} = 900$)	0.11	0.21	1.07×10^{-5}
BP3 ($M_{H_F} = 1000$)	0.12	0.11	6.23×10^{-6}

TABLE VIII. The matched cross sections for the most relevant SM background processes. (Note that these background rates will be multiplied by the fake rates during the analysis.)

SM backgrounds	Cross section (pb)
$pp \to ZZ$jets (up to 3 jets)	11.64
$pp \to t\bar{t}Z$jets (up to 2 jets)	0.76
$pp \to VVV(V = W/Z)$jets (up to 2 jets)	1.04
$pp \to VH$jets (up to 3 jets)	0.69
$pp \to WZ$jets (up to 3 jets)	40.10
$pp \to WW$jets (up to 3 jets)	89.20
$pp \to t\bar{t}$jets (up to 2 jets)	915.10

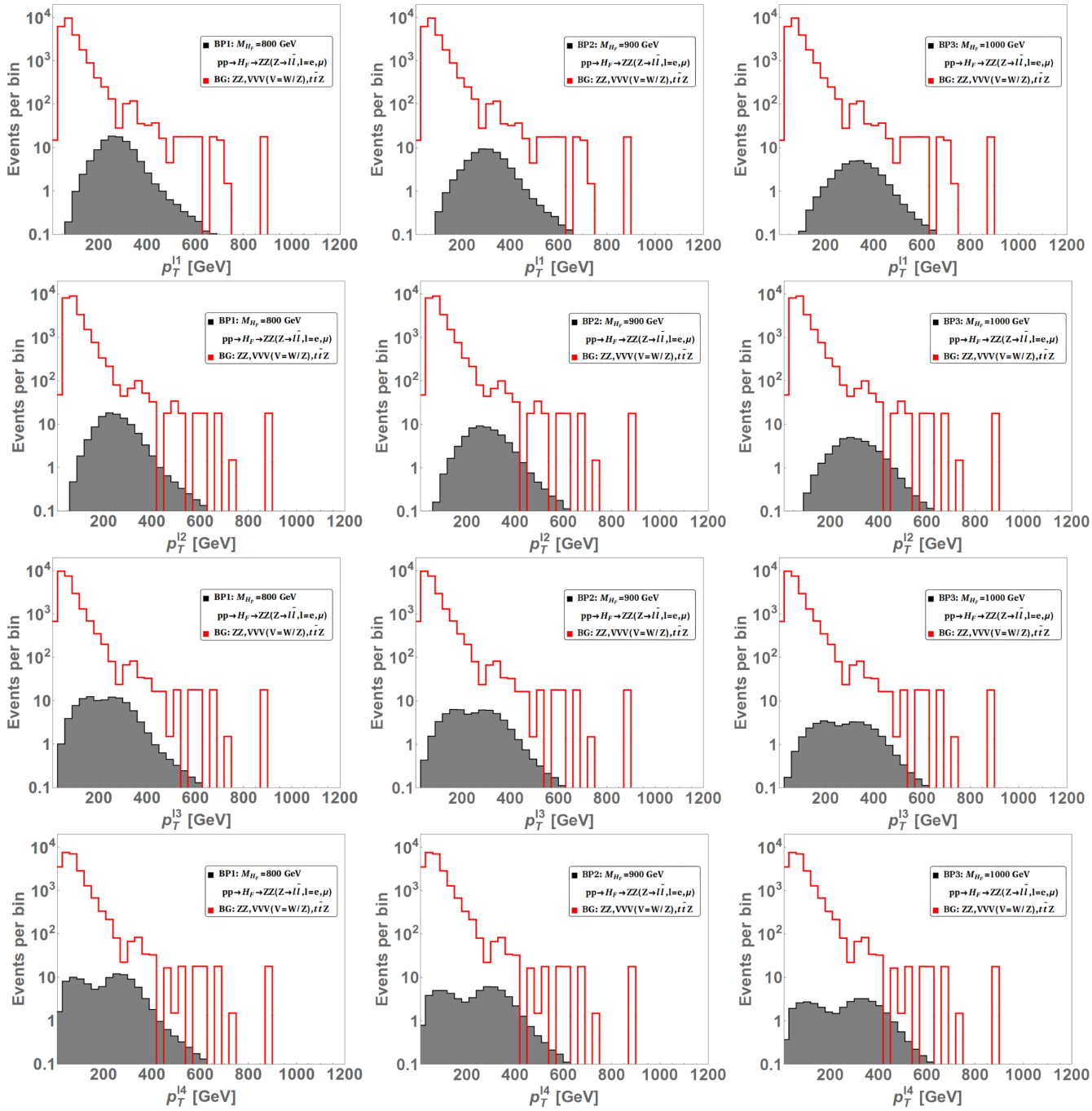

FIG. 16. Transverse momentum distributions for signal and total background after the acceptance cuts.

The calculations were performed for a center-of-mass energy of $\sqrt{s} = 14$ TeV and an integrated luminosity of $\mathcal{L} = 3000$ fb^{-1}. We calculate the signal significance using the formula $\sigma = \frac{S}{\sqrt{S+B}}$, where S represents the signal yield and B represents the background yield.

C. $pp \to \phi \to tc$ $(t \to b\ell\nu_\ell)$, $\phi = H_F, A_F$

1. $pp \to H_F \to tc$

The presence of nonzero $\tilde{Z}_{tc}$ allows for processes such as $\phi \to tc$, where ϕ decays into a top quark and an anticharm

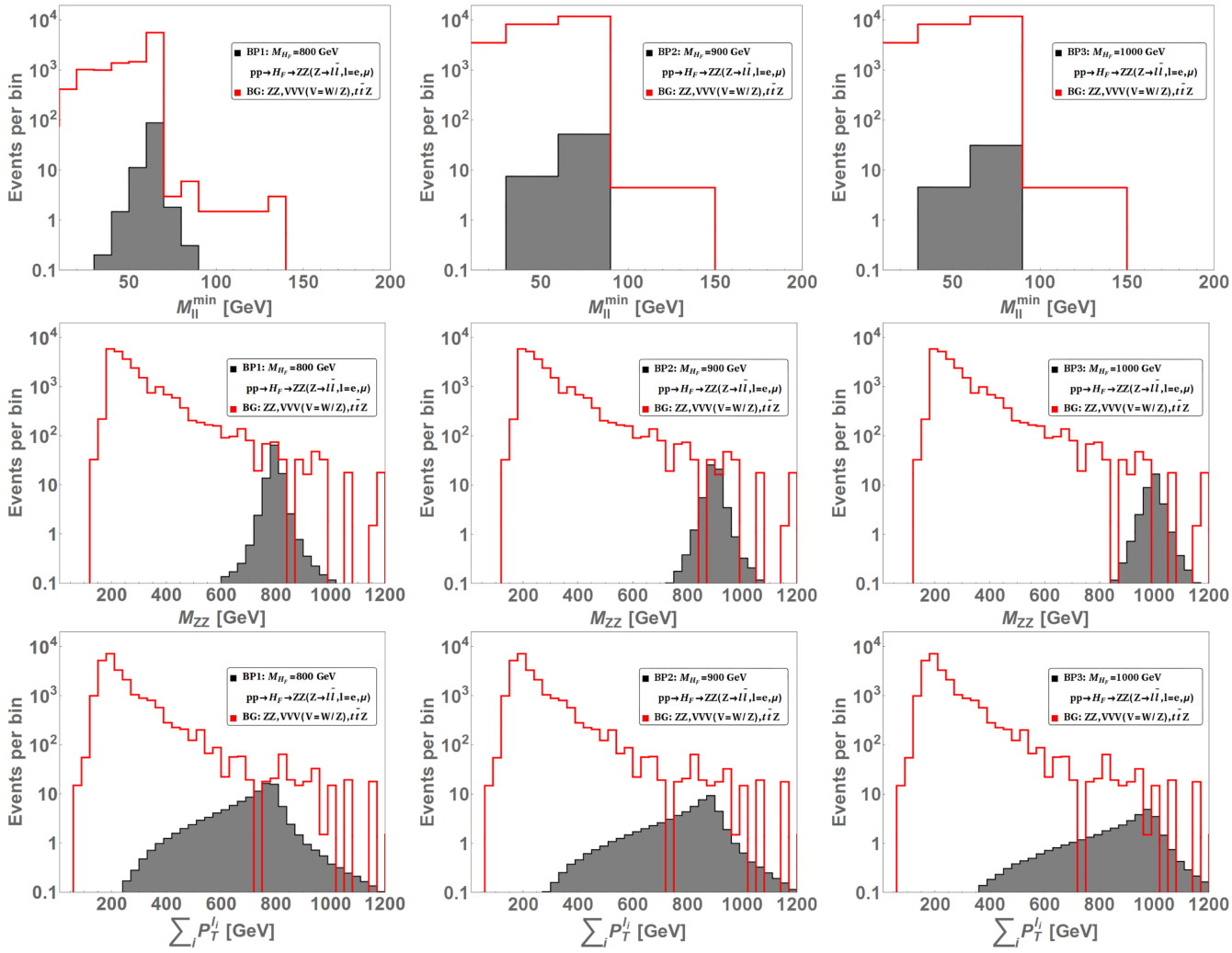

FIG. 17. Invariant mass of two leptons, four leptons, sum of all momentum distributions for signal and total background after the acceptance cuts.

quark, or a charm quark and an antitop quark, respectively. These flavor-violating decays are possible due to the mixing between the top and charm quarks induced by the nonzero $\tilde{Z}_{tc}$. The observation of such flavor-violating decays would have significant implications for our understanding of the FN heavy Higgs sector. It would provide evidence for new physics beyond the SM, as the SM predicts negligible flavor violation in the Higgs sector. The presence of flavor-violating decays would suggest the existence of new particles or interactions that can induce such processes.

Studying the properties of the flavor-violating decays, such as their rates and kinematic distributions, can provide valuable information about the underlying physics responsible for the FN-heavy Higgs sector. It can help constrain the model's parameter space and provide insights into the flavor structure and dynamics of the theory. We present the analysis for the production of the $\phi = H_F, A_F$ via proton-proton collisions $pp \to \phi$, followed by the FCNC decay $\phi \to tc$ $(t \to b\ell\nu_\ell)$ in the presence of nonzero $\tilde{Z}_{tc}$. The model parameter values used in the simulation are shown in Table XI. We present in Fig. 18 a general overview of the number of events produced $N_S = \sigma(pp \to \phi \to tc(t \to b\ell\nu_\ell)) \times \mathcal{L}_{\text{int}}$, with $\mathcal{L}_{\text{int}} = 300\ \text{fb}^{-1}$. We notice that the number of events of both

TABLE IX. The optimized SR as a function of the H_F mass.

	Kinematic variables and cuts	
	Observable	Value
SR	$p_T^{\ell_{1,2,3,4}}$	>35 (GeV)
	$\sum_i p_T^{\ell_i}$	>180 (GeV)
	M_{ZZ} (varied with M_{H_F})	$0.95M_{H_F} - 1.05M_{H_F}$

TABLE X. The signal significance $\sigma = \frac{S}{\sqrt{S+B}}$ for BP1, BP2, and BP3 corresponding to the optimized SR are shown. In addition, the total background yield and the total signal yield are also given at $\sqrt{s} = 14$ TeV with integrated luminosity $\mathcal{L} = 3000$ fb^{-1}.

Benchmark points: Signal and significances								
BP1 ($M_{H_F} = 800$ GeV)			BP2 ($M_{H_F} = 900$ GeV)			BP3 ($M_{H_F} = 1000$ GeV)		
Number of signal	Number of background	Significance	Number of signal	Number of background	Significance	Number of signal	Number of background	Significance
90.42	83.67	6.83	51.48	27.98	5.78	51.77	66.95	4.75

signals is close in regimenes of intermediate and high masses. The reason is because we have found that $\sigma(pp \to A_F) \sim 10^{-2}\sigma(pp \to H_F)$ and $\mathrm{BR}(A_F \to tc) \sim 10\,\mathrm{BR}(H_F \to tc)$, as shown in Tables XII–XIV.

On the other hand, the $\mathrm{BR}(H_F \to tc)$ as a function of the singlet VEV v_s and the $\tilde{Z}_{tc}$ matrix element is shown in Fig. 19. We observe $\mathrm{BRs}(H_F \to tc)$ quite large $\mathcal{O}(0.1)$, which comes because the couplings $H_F WW$ and $H_F ZZ$ are suppressed, which allows the opening of the tc channel.

In this analysis, the main SM background comes from the final state of $bj\ell\nu_\ell$, whose source arises mainly from $Wjj + Wb\bar{b}$, $tb + tj$. Another important background is $t\bar{t}$ production, where either one of the two leptons is missed in the semileptonic top quark decays, or two of the four jets are missed when one of the top quarks decays semileptonically. The cross sections of the dominant SM background are shown in Table XIII.

Figure 20 shows the kinematic distributions generated both by the signal (for $M_{H_F} = 800$ GeV, $v_s = 1000$ GeV) and background processes, namely, the transverse momentum of the particles produced by the decay of the top quark: (a) leading b-jet, (b) the charged lepton, (c) the missing energy transverse (MET) due to the neutrino in the final state. The transverse momentum of the leading light jet is shown in (d). A remarkable fact is the difference in

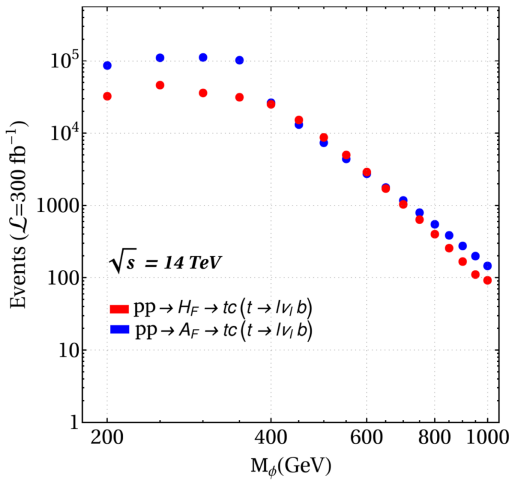

FIG. 18. Number of events produced for the process $pp \to \phi \to tc(t \to \ell\nu_\ell b)$.

TABLE XI. Model parameter values used in the Monte Carlo simulation.

Parameter	Value
c_α	0.995
v_s	600–1000 (GeV)
$\tilde{Z}_{tc}$	0.1
$M_{H_F} = M_{A_F}$	800–1000 (GeV)

TABLE XII. The $\mathrm{BR}(H_F \to tc)$ and cross sections for the processes $pp \to H_F$ and $\sigma(pp \to H_F \to tc, t \to \ell\nu_\ell b)$ for three BPs (BP1, BP2 and BP3) used in the remainder of the paper.

	BRs and cross sections (pb)		
BPs (GeV)	$\mathrm{BR}(H_F \to tc)$	$\sigma(pp \to H_F)$	$\sigma(pp \to H_F \to tc, t \to \ell\nu_\ell b)$
BP1 ($M_{H_F} = 800$)	0.0140	0.41	1.34×10^{-3}
BP2 ($M_{H_F} = 900$)	0.0134	0.21	6.23×10^{-4}
BP3 ($M_{H_F} = 1000$)	0.0133	0.11	3.32×10^{-4}

TABLE XIII. Cross section of the dominant SM background processes.

SM backgrounds	Cross section (pb)
$pp \to Wjj + Wb\bar{b}(W \to \ell\nu_\ell)$	3245
$pp \to tb + tj(t \to \ell\nu_\ell b)$	1.61
$pp \to t\bar{t}(t \to \ell\nu_\ell b, t \to q_i q_j b)$	65.50

TABLE XIV. The $\mathrm{BR}(H_F \to tc)$ and cross sections for the processes $pp \to H_F$ and $\sigma(pp \to H_F \to tc, t \to \ell\nu_\ell b)$ for three BPs (BP1, BP2 and BP3) used in the remainder of the paper.

	BRs and cross sections (pb)		
BPs (GeV)	$\mathrm{BR}(A_F \to tc)$	$\sigma(pp \to A_F)$	$\sigma(pp \to A_F \to tc, t \to \ell\nu_\ell b)$
BP1 ($M_{A_F} = 800$)	0.4980	0.0176	1.97×10^{-3}
BP2 ($M_{A_F} = 900$)	0.4973	0.0086	9.67×10^{-4}
BP3 ($M_{A_F} = 1000$)	0.4970	0.0042	4.70×10^{-4}

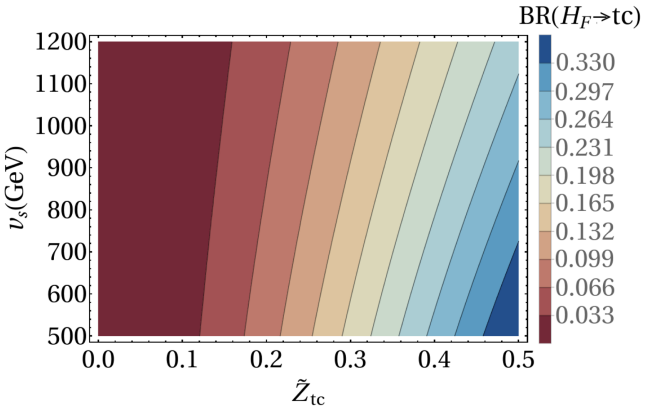

FIG. 19. BR($H_F \to tc$) as a function of the singlet VEV v_s and the $\tilde{Z}_{tc}$ matrix element.

transverse masses between the background and signal processes. So, we present in Fig. 21 the transverse mass for both reactions, which is the most important confirmation of the signal.

The following acceptance and kinematic cuts imposed to study possible evidence of the $H_F \to tc$ ($M_{H_F} = 800$ GeV) at the LHC are as follows:

(i) We requiere two jets with $|\eta^j| < 2.5$ and $p_T^j >$ 30 GeV, one of them is tagged as a b-jet.
(ii) We require one isolated lepton (e or μ) with $|\eta^\ell| <$ 2.5 and $p_T^\ell > 30$ GeV.
(iii) Since an undetected neutrino is included in the final state, we impose the cut MET > 40 GeV.

Finally, we impose a cut on the transverse mass $M^T \equiv M^T_{\ell \not{E}_T} = \sqrt{2 p_l^T \not{E}_T (1 - \cos\phi_{\ell \not{E}_T})}$ as $|M^T - M_{H_F}| < 50$ GeV to enhance the signals.

Figure 22 displays the contour plots of the signal significance as a function of the integrated luminosity $\mathcal{L}_{\rm int}$ and the singlet scalar VEV v_s, for $M_{H_F} = 800$ GeV, 900 GeV, 1000 GeV. Once $\mathcal{L}_{\rm int} = 300$ fb^{-1} of accumulated data is achieved and assuming $v_s = 640$ GeV (625 GeV, 620 GeV), we find that the LHC would have the possibility of exploring a detectable flavon H_F of mass 800 GeV

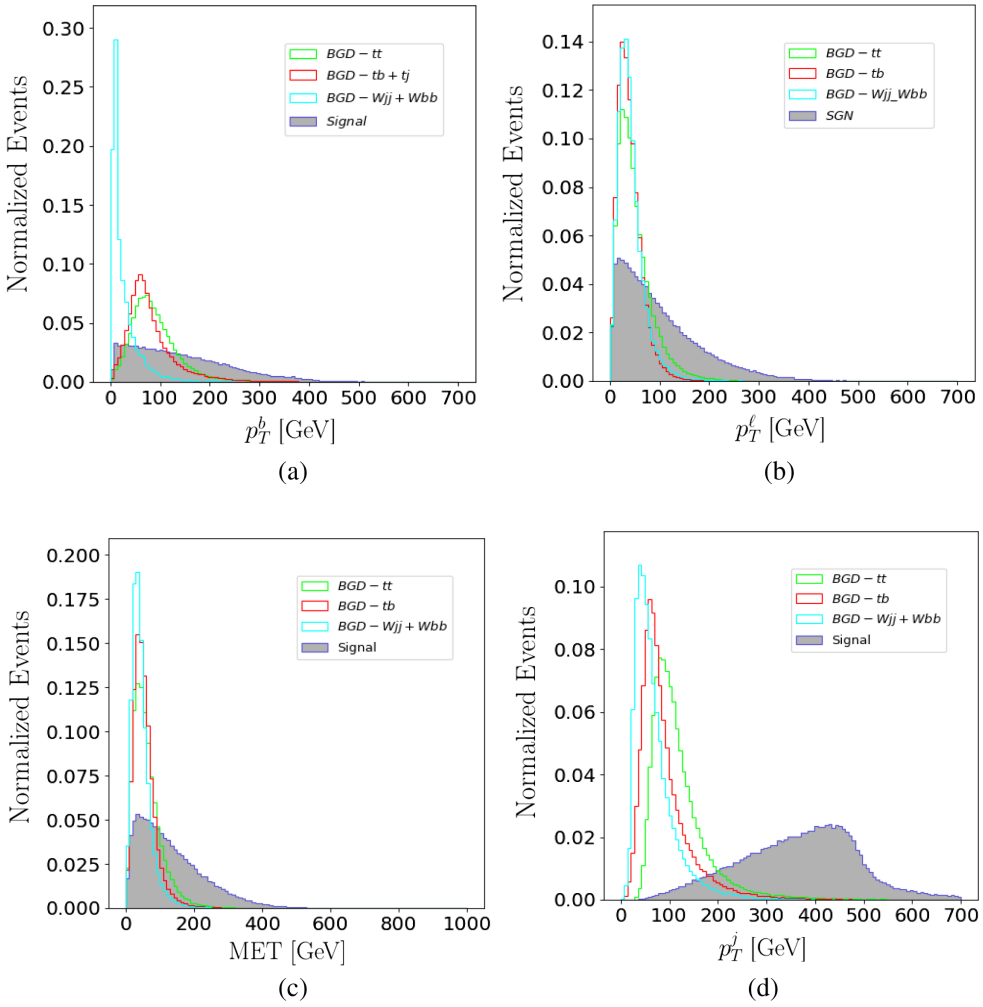

FIG. 20. Normalized transverse momentum distributions associated to the top decay: (a) leading b-jet; (b) leading charged lepton, (c) tranverse missing energy due to undetected neutrinos; (d) transverse momentum distribution of the c-jet.

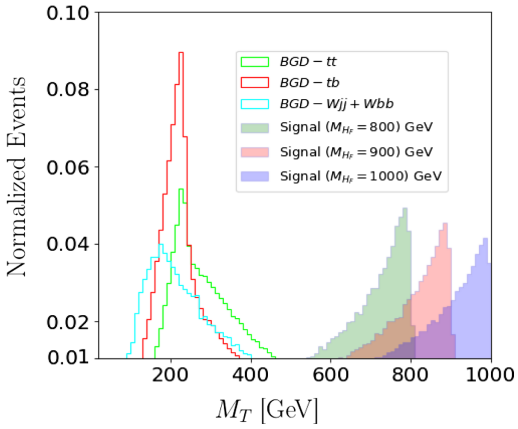

FIG. 21. Normalized transverse mass $M^T = \sqrt{2p_\ell^T \not{E}_T(1-\cos\phi_{\ell\not{E}_T})}$ for both background and signal processes. We have considered $M_{H_F} = 800$ GeV, 900 GeV, 1000 GeV.

(900 GeV, 1000 GeV). Even more promising results could be found in the HL-LHC era, which could corroborate the possible findings of the LHC regarding the $H_F \to tc$ process.

2. $pp \to A_F \to tc$

As far as the decay $A_F \to tc$ is concerned, we proceed in a similar way to the previous analysis. Here is relevant show the main decay modes of the flavon A_F in order to highlight the signal sought. Figure 23(a) shows the BR$(A_F \to XX)$-M_{A_F} plane for processes that arise at tree level. We notice that the dominant production channels, assuming intermediate masses, are $A_F \to tt$ and $A_F \to tc$ which are of order $\mathcal{O}(10^{-1})$. It is because the flavon A_F does not couples to the gauge boson W and Z. Meanwhile, Fig. 23(b) shows the two-body decays at one-loop level, in which we observe that the dominant channel is the one into two gluons. Once the Monte Carlo analyis was done, we found an increase of ∼6% in the signal significance of the

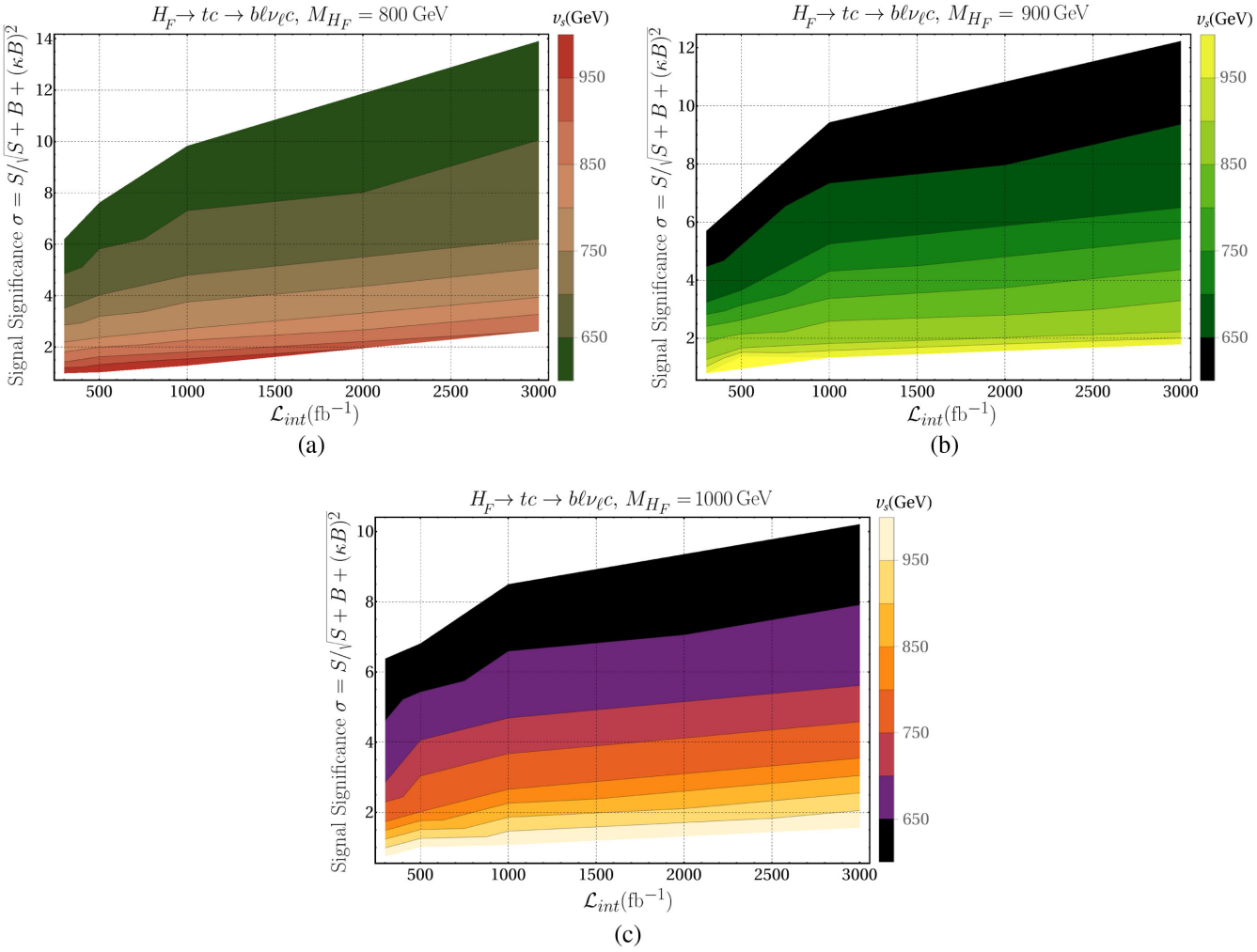

FIG. 22. Contour plots for the signal significance as a function of the integrated luminosity and the singlet VEV v_s. (a) $M_{H_F} = 800$ GeV, (b) $M_{H_F} = 900$ GeV, (c) $M_{H_F} = 1000$ GeV. In these results we consider a systematic uncertainty $\kappa = 5\%$.

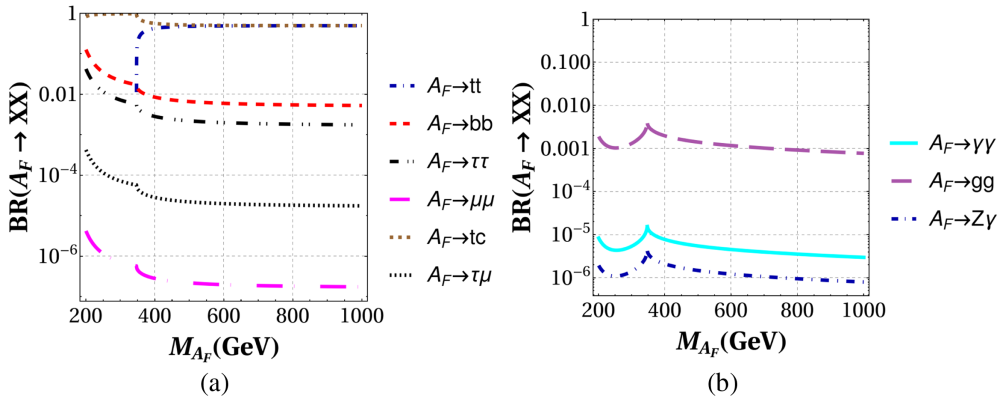

FIG. 23. Branching ratios of the main decay modes of A_F as a function of its mass M_{A_F}, (a) at tree level and (b) at one-loop level.

process $A_F \to tc$ with respect to the signal $H_F \to tc$. Although the signal is similar, the $\phi \to tc$ process could be distinguished by the number of events produced.

V. CONCLUSIONS

The hierarchical structure and peculiar pattern of quark and lepton masses in the SM have been a long standing issue coined as the 'flavor puzzle'. Various interesting beyond the SM proposals have been suggested to resolve this riddle. Among these, the one by Froggatt and Nielsen is arguably one of the most fascinating ones. Herein, the scalar sector predicts one singlet complex scalar S_F which is charged under a new $U(1)_F$ flavor symmetry (which is softly broken). After EWSB and $U(1)_F$ breaking, the mixing between the SM Higgs doublet with the real part of the S_F singlet produces two physical scalars, h and H_F, where h is identified as the SM-like Higgs boson (discovered in 2012) while H_F is an additional CP-even (so-called) flavon with mass $\mathcal{O}(1\ \text{TeV})$. (The imaginary part of S_F is identified as the CP-odd heavy flavon A_F.) The (pseudo)scalar sector of this model is controlled by two parameters; the flavon VEV v_s and the mixing angle α. The structure of various Yukawa couplings of this model is such that one can have FCNCs involving the two new heavy (pseudo)scalars (H_F and A_F) even at tree level. The corresponding contributions to FCNC processes thus attract severe constraints from various low-energy flavor physics data. Therefore, in our analysis of such a scenario, we have considered all possible experimental (as well as theoretical) limits on the model parameters v_s and α. With the LHC currently running at CERN, it is very tempting to utilize the ongoing (Run 3) and future (HL-LHC) stages of the machine to explore the signature of such heavy flavons.

In this paper, our primary focus was on the CP-even heavy flavon denoted as H_F. We explored its discovery potential at the LHC by investigating its production through gluon-gluon fusion followed by its subsequent decays. We considered various decay modes for it, including into two SM Higgs bosons and two SM (neutral) gauge bosons. By studying these different decay channels and considering the corresponding signatures at HL-LHC (with $\sqrt{s} = 14$ TeV), assuming a luminosity of 3000 fb^{-1}, we were able to confirm the discovery potential (5σ) of the CP-even heavy flavon H_F at the LHC through these SM signatures. In addition, we explored the flavor-changing $\phi \to tc$ decays ($\phi = A_F, H_F$), specific to our model, which is predicted to arise when $M_\phi \gtrsim m_t$. The branching ratio of these decays can be as large as $\mathcal{O}(0.1)$ because the $H_F \to VV$ ($V = W, Z$) decays are suppressed once the tc channel is opened and because A_F does not couple to VV. We have found that these non-SM channels offer an alternative opportunity to test our model, even at the LHC. It is to be noted that the CP-even H_F and CP-odd A_F scalars can exhibit similar signatures in the HF → tc and AF → tc decay channels when they have the same masses. Nevertheless, additional di-Higgs and digauge boson production channels can offer valuable discriminating power between these two scalar particles. Once an integrated luminosity of 300 fb^{-1} is achieved, we predict a signal significance of up to 6σ for masses of the flavons between 800–1000 GeV.

We have obtained such results following a thorough numerical analysis emulating both the aforementioned signal and the most relevant (ir)reducible backgrounds accounting for hard scattering, parton shower, hadronization, and detector effects. We thus advocate that the experimental collaborations at the LHC, specifically, the multipurpose ones (ATLAS and CMS), tackle this search, as its results can lead to a better understanding of the origin and solution of the flavor puzzle in the SM. This should be facilitated by having implemented the advocated model in standard computational tools, which are available upon request.

ACKNOWLEDGMENTS

S. M. acknowledges funding from the STFC Consolidated Grant No. ST/L000296/1 and is partially supported through the NExT Institute. N. K. would like to acknowledge support from the DAE, Government of India

and the Regional Centre for Accelerator-based Particle Physics (RECAPP), HRI (HRI-RECAPP-2023-05). The work of M. A. A.-U. is supported by "Estancias posdoctorales por México (CONACYT)". J. L. D-C. acknowledges the support of SNI (Mexico) and VIEP (BUAP). The work of A. C. is funded by the Department of Science and Technology, Government of India, under Grant No. IFA18PH224 (INSPIRE Faculty Award).

[1] G. Aad *et al.* (ATLAS Collaboration), Observation of a new particle in the search for the Standard Model Higgs boson with the ATLAS detector at the LHC, Phys. Lett. B **716**, 1 (2012).

[2] S. Chatrchyan *et al.* (CMS Collaboration), Observation of a new boson at a mass of 125 GeV with the CMS experiment at the LHC, Phys. Lett. B **716**, 30 (2012).

[3] P. P. Giardino, K. Kannike, I. Masina, M. Raidal, and A. Strumia, The universal Higgs fit, J. High Energy Phys. 05 (2014) 046.

[4] A. M. Sirunyan *et al.* (CMS Collaboration), Observation of the Higgs boson decay to a pair of τ leptons with the CMS detector, Phys. Lett. B **779**, 283 (2018).

[5] A. M. Sirunyan *et al.* (CMS Collaboration), Combined measurements of Higgs boson couplings in proton–proton collisions at $\sqrt{s} = 13$ TeV, Eur. Phys. J. C **79**, 421 (2019).

[6] Z. Kunszt, S. Moretti, and W. J. Stirling, Higgs production at the LHC: An update on cross-sections and branching ratios, Z. Phys. C **74**, 479 (1997).

[7] S. Dawson, S. Dittmaier, and M. Spira, Neutral Higgs boson pair production at hadron colliders: QCD corrections, Phys. Rev. D **58**, 115012 (1998).

[8] J. Baglio, F. Campanario, S. Glaus, M. Mühlleitner, M. Spira, and J. Streicher, Gluon fusion into Higgs pairs at NLO QCD and the top mass scheme, Eur. Phys. J. C **79**, 459 (2019).

[9] J. Baglio, F. Campanario, S. Glaus, M. Mühlleitner, J. Ronca, M. Spira, and J. Streicher, Higgs-pair production via gluon fusion at hadron colliders: NLO QCD corrections, J. High Energy Phys. 04 (2020) 181.

[10] M. Aaboud *et al.* (ATLAS Collaboration), Search for heavy ZZ resonances in the $\ell^+\ell^-\ell^+\ell^-$ and $\ell^+\ell^-\nu\bar{\nu}$ final states using proton–proton collisions at $\sqrt{s} = 13$ TeV with the ATLAS detector, Eur. Phys. J. C **78**, 293 (2018).

[11] J. Baglio, L. D. Ninh, and M. M. Weber, Massive gauge boson pair production at the LHC: A next-to-leading order story, Phys. Rev. D **88**, 113005 (2013); **94**, 099902(E) (2016).

[12] A. Adhikary, S. Banerjee, R. K. Barman, B. Bhattacherjee, and S. Niyogi, Revisiting the non-resonant Higgs pair production at the HL-LHC, J. High Energy Phys. 07 (2018) 116.

[13] G. Aad *et al.* (ATLAS Collaboration), Search for heavy resonances decaying into a pair of Z bosons in the $\ell^+\ell^-\ell'^+\ell'^-$ and $\ell^+\ell^-\nu\bar{\nu}$ final states using 139 fb^{-1} of proton–proton collisions at $\sqrt{s} = 13$ TeV with the ATLAS detector, Eur. Phys. J. C **81**, 332 (2021).

[14] J. Baglio, A. Djouadi, R. Gröber, M. M. Mühlleitner, J. Quevillon, and M. Spira, The measurement of the Higgs self-coupling at the LHC: Theoretical status, J. High Energy Phys. 04 (2013) 151.

[15] V. Barger, L. L. Everett, C. B. Jackson, and G. Shaughnessy, Higgs-pair production and measurement of the triscalar coupling at LHC(8,14), Phys. Lett. B **728**, 433 (2014).

[16] N. Kumar and S. P. Martin, LHC search for di-Higgs decays of stoponium and other scalars in events with two photons and two bottom jets, Phys. Rev. D **90**, 055007 (2014).

[17] A. Adhikary, S. Banerjee, R. Kumar Barman, and B. Bhattacherjee, Resonant heavy Higgs searches at the HL-LHC, J. High Energy Phys. 09 (2019) 068.

[18] A. Adhikary, R. K. Barman, and B. Bhattacherjee, Prospects of non-resonant di-Higgs searches and Higgs boson self-coupling measurement at the HE-LHC using machine learning techniques, J. High Energy Phys. 12 (2020) 179.

[19] J. Baglio, O. Eberhardt, U. Nierste, and M. Wiebusch, Benchmarks for Higgs pair production and heavy Higgs boson searches in the two-Higgs-doublet model of Type II, Phys. Rev. D **90**, 015008 (2014).

[20] B. Hespel, D. Lopez-Val, and E. Vryonidou, Higgs pair production via gluon fusion in the two-Higgs-doublet model, J. High Energy Phys. 09 (2014) 124.

[21] L.-C. Lü, C. Du, Y. Fang, H.-J. He, and H. Zhang, Searching heavier Higgs boson via di-Higgs production at LHC Run-2, Phys. Lett. B **755**, 509 (2016).

[22] G. D. Kribs and A. Martin, Enhanced di-Higgs production through light colored scalars, Phys. Rev. D **86**, 095023 (2012).

[23] L. Bian and N. Chen, Higgs pair productions in the *CP*-violating two-Higgs-doublet model, J. High Energy Phys. 09 (2016) 069.

[24] S. Dawson, E. Furlan, and I. Lewis, Unravelling an extended quark sector through multiple Higgs production?, Phys. Rev. D **87**, 014007 (2013).

[25] A. Pierce, J. Thaler, and L.-T. Wang, Disentangling dimension six operators through di-Higgs boson production, J. High Energy Phys. 05 (2007) 070.

[26] S. Kanemura and K. Tsumura, Effects of the anomalous Higgs couplings on the Higgs boson production at the Large Hadron Collider, Eur. Phys. J. C **63**, 11 (2009).

[27] U. Ellwanger, Higgs pair production in the NMSSM at the LHC, J. High Energy Phys. 08 (2013) 077.

[28] C.-R. Chen and I. Low, Double take on new physics in double Higgs boson production, Phys. Rev. D **90**, 013018 (2014).
[29] N. Liu, S. Hu, B. Yang, and J. Han, Impact of top-Higgs couplings on di-Higgs production at future colliders, J. High Energy Phys. 01 (2015) 008.
[30] F. Goertz, A. Papaefstathiou, L. L. Yang, and J. Zurita, Higgs boson pair production in the $D = 6$ extension of the SM, J. High Energy Phys. 04 (2015) 167.
[31] A. Azatov, R. Contino, G. Panico, and M. Son, Effective field theory analysis of double Higgs boson production via gluon fusion, Phys. Rev. D **92**, 035001 (2015).
[32] M. J. Dolan, C. Englert, and M. Spannowsky, New physics in LHC Higgs boson pair production, Phys. Rev. D **87**, 055002 (2013).
[33] V. Barger, L. L. Everett, C. B. Jackson, A. D. Peterson, and G. Shaughnessy, New physics in resonant production of Higgs boson pairs, Phys. Rev. Lett. **114**, 011801 (2015).
[34] A. Crivellin, M. Ghezzi, and M. Procura, Effective field theory with two Higgs doublets, J. High Energy Phys. 09 (2016) 160.
[35] H. Sun, Y.-J. Zhou, and H. Chen, Constraints on large-extra-dimensions model through 125-GeV Higgs pair production at the LHC, Eur. Phys. J. C **72**, 2011 (2012).
[36] R. Costa, M. Mühlleitner, M. O. P. Sampaio, and R. Santos, Singlet extensions of the standard model at LHC run 2: Benchmarks and comparison with the NMSSM, J. High Energy Phys. 06 (2016) 034.
[37] K. Cheung, A. Jueid, C.-T. Lu, J. Song, and Y. W. Yoon, Disentangling new physics effects on nonresonant Higgs boson pair production from gluon fusion, Phys. Rev. D **103**, 015019 (2021).
[38] A. Alves, D. Gonçalves, T. Ghosh, H.-K. Guo, and K. Sinha, Di-Higgs production in the 4b channel and gravitational wave complementarity, J. High Energy Phys. 03 (2020) 053.
[39] C. Englert and J. Jaeckel, Probing the symmetric Higgs portal with di-Higgs boson production, Phys. Rev. D **100**, 095017 (2019).
[40] P. Basler, S. Dawson, C. Englert, and M. Mühlleitner, Showcasing HH production: Benchmarks for the LHC and HL-LHC, Phys. Rev. D **99**, 055048 (2019).
[41] Z. Heng, X. Gong, and H. Zhou, Pair production of Higgs boson in NMSSM at the LHC with the next-to-lightest CP-even Higgs boson being SM-like, Chin. Phys. C **42**, 073103 (2018).
[42] B. Das, S. Moretti, S. Munir, and P. Poulose, Quantum interference effects in Higgs boson pair-production beyond the Standard Model, Eur. Phys. J. C **81**, 347 (2021).
[43] H. Abouabid, A. Arhrib, D. Azevedo, J. E. Falaki, P. M. Ferreira, M. Mühlleitner, and R. Santos, Benchmarking di-Higgs production in various extended Higgs sector models, J. High Energy Phys. 09 (2022) 011.
[44] S. Dasgupta, R. Pramanick, and T. S. Ray, Broad toplike vector quarks at LHC and HL-LHC, Phys. Rev. D **105**, 035032 (2022).
[45] L. Huang, S.-b. Kang, J. H. Kim, K. Kong, and J. S. Pi, Portraying double Higgs at the Large Hadron Collider II, J. High Energy Phys. 08 (2022) 114.
[46] G. Li, L.-X. Xu, B. Yan, and C. P. Yuan, Resolving the degeneracy in top quark Yukawa coupling with Higgs pair production, Phys. Lett. B **800**, 135070 (2020).
[47] Q.-H. Cao, B. Yan, D.-M. Zhang, and H. Zhang, Resolving the degeneracy in single Higgs production with Higgs pair production, Phys. Lett. B **752**, 285 (2016).
[48] Q.-H. Cao, G. Li, B. Yan, D.-M. Zhang, and H. Zhang, Double Higgs production at the 14 TeV LHC and a 100 TeV pp collider, Phys. Rev. D **96**, 095031 (2017).
[49] J. Cao, D. Li, L. Shang, P. Wu, and Y. Zhang, Exploring the Higgs sector of a most natural NMSSM and its prediction on Higgs pair production at the LHC, J. High Energy Phys. 12 (2014) 026.
[50] J. Cao, Z. Heng, L. Shang, P. Wan, and J. M. Yang, Pair production of a 125 GeV Higgs boson in MSSM and NMSSM at the LHC, J. High Energy Phys. 04 (2013) 134.
[51] C.-T. Lu, J. Chang, K. Cheung, and J. S. Lee, An exploratory study of Higgs-boson pair production, J. High Energy Phys. 08 (2015) 133.
[52] J. Kopp, Flavor violation in the scalar sector, in *Proceedings of the 51st Rencontres de Moriond on EW Interactions and Unified Theories* (2016), pp. 281–288, arXiv:1605.02865.
[53] E. Arganda, X. Marcano, N. I. Mileo, R. A. Morales, and A. Szynkman, Model-independent search strategy for the lepton-flavor-violating heavy Higgs boson decay to $\tau\mu$ at the LHC, Eur. Phys. J. C **79**, 738 (2019).
[54] B. Altunkaynak, W.-S. Hou, C. Kao, M. Kohda, and B. McCoy, Flavor changing heavy Higgs interactions at the LHC, Phys. Lett. B **751**, 135 (2015).
[55] I. Doršner, S. Fajfer, A. Greljo, J. F. Kamenik, and N. Košnik, Physics of leptoquarks in precision experiments and at particle colliders, Phys. Rep. **641**, 1 (2016).
[56] A. Davidson, V. P. Nair, and K. C. Wali, Peccei-Quinn symmetry as flavor symmetry and grand unification, Phys. Rev. D **29**, 1504 (1984).
[57] A. Davidson and K. C. Wali, Minimal flavor unification via multigenerational Peccei-Quinn symmetry, Phys. Rev. Lett. **48**, 11 (1982).
[58] C. D. Froggatt and H. B. Nielsen, Hierarchy of quark masses, Cabibbo angles and CP violation, Nucl. Phys. **B147**, 277 (1979).
[59] A. Bolaños, J. L. Diaz-Cruz, G. Hernández-Tomé, and G. Tavares-Velasco, Has a Higgs-flavon with a 750 GeV mass been detected at the LHC13?, Phys. Lett. B **761**, 310 (2016).
[60] M. Bauer, T. Schell, and T. Plehn, Hunting the flavon, Phys. Rev. D **94**, 056003 (2016).
[61] K. Huitu, V. Keus, N. Koivunen, and O. Lebedev, Higgs-flavon mixing and $h \to \mu\tau$, J. High Energy Phys. 05 (2016) 026.
[62] E. L. Berger, S. B. Giddings, H. Wang, and H. Zhang, Higgs-flavon mixing and LHC phenomenology in a simplified model of broken flavor symmetry, Phys. Rev. D **90**, 076004 (2014).
[63] J. L. Diaz-Cruz and U. J. Saldaña Salazar, Higgs couplings and new signals from Flavon–Higgs mixing effects within multi-scalar models, Nucl. Phys. **B913**, 942 (2016).
[64] M. A. Arroyo-Ureña, J. L. Díaz-Cruz, G. Tavares-Velasco, A. Bolaños, and G. Hernández-Tomé, Searching for lepton

flavor violating flavon decays at hadron colliders, Phys. Rev. D **98**, 015008 (2018).
[65] M. A. Arroyo-Ureña, A. Fernández-Téllez, and G. Tavares-Velasco, Flavor changing flavon decay $\phi \to tc$ $(\phi = H_F, A_F)$ at the high luminosity large hadron collider, Rev. Mex. Fis. **69**, 020803 (2023).
[66] K. Tsumura and L. Velasco-Sevilla, Phenomenology of flavon fields at the LHC, Phys. Rev. D **81**, 036012 (2010).
[67] F. Gianotti *et al.*, Physics potential and experimental challenges of the LHC luminosity upgrade, Eur. Phys. J. C **39**, 293 (2005).
[68] G. Apollinari, O. Brüning, T. Nakamoto, and L. Rossi, High luminosity Large Hadron Collider HL-LHC, CERN Yellow Rep. 1 (2015).
[69] G. Aad *et al.* (ATLAS Collaboration), Combination of searches for Higgs boson pairs in pp collisions at $\sqrt{s} =$ 13 TeV with the ATLAS detector, Phys. Lett. B **800**, 135103 (2020).
[70] M. Aaboud *et al.* (ATLAS Collaboration), Search for Higgs boson pair production in the $WW^{(*)}WW^{(*)}$ decay channel using ATLAS data recorded at $\sqrt{s} = 13$ TeV, J. High Energy Phys. 05 (2019) 124.
[71] M. Aaboud *et al.* (ATLAS Collaboration), Search for Higgs boson pair production in the $b\bar{b}WW^*$ decay mode at $\sqrt{s} = 13$ TeV with the ATLAS detector, J. High Energy Phys. 04 (2019) 092.
[72] M. Aaboud *et al.* (ATLAS Collaboration), Search for resonant and non-resonant Higgs boson pair production in the $b\bar{b}\tau^+\tau^-$ decay channel in pp collisions at $\sqrt{s} =$ 13 TeV with the ATLAS detector, Phys. Rev. Lett. **121**, 191801 (2018); **122**, 089901(E) (2019).
[73] A. M. Sirunyan *et al.* (CMS Collaboration), Search for Higgs boson pair production in events with two bottom quarks and two tau leptons in proton–proton collisions at $\sqrt{s} = 13$ TeV, Phys. Lett. B **778**, 101 (2018).
[74] M. Aaboud *et al.* (ATLAS Collaboration), Search for Higgs boson pair production in the $\gamma\gamma WW^*$ channel using pp collision data recorded at $\sqrt{s} = 13$ TeV with the ATLAS detector, Eur. Phys. J. C **78**, 1007 (2018).
[75] M. Aaboud *et al.* (ATLAS Collaboration), Search for Higgs boson pair production in the $\gamma\gamma b\bar{b}$ final state with 13 TeV pp collision data collected by the ATLAS experiment, J. High Energy Phys. 11 (2018) 040.
[76] M. Aaboud *et al.* (ATLAS Collaboration), Search for pair production of Higgs bosons in the $b\bar{b}b\bar{b}$ final state using proton-proton collisions at $\sqrt{s} = 13$ TeV with the ATLAS detector, J. High Energy Phys. 01 (2019) 030.
[77] A. M. Sirunyan *et al.* (CMS Collaboration), Combination of searches for Higgs boson pair production in proton-proton collisions at $\sqrt{s} = 13$ TeV, Phys. Rev. Lett. **122**, 121803 (2019).
[78] ATLAS Collaboration, Constraints on the Higgs boson self-coupling from the combination of single-Higgs and double-Higgs production analyses performed with the ATLAS experiment, Report No. ATLAS-CONF-2019-049, 2019.
[79] ATLAS Collaboration, Measurement and interpretation of same-sign W boson pair production in association with two jets in pp collisions at $\sqrt{s} = 13$ TeV with the ATLAS detector, Report No. ATLAS-CONF-2023-023, 2023.
[80] G. Aad *et al.* (ATLAS Collaboration), Evidence of off-shell Higgs boson production from ZZ leptonic decay channels and constraints on its total width with the ATLAS detector, Phys. Lett. B **846**, 138223 (2023).
[81] D. Zubov, D. Pyatiizbyantseva, and E. Soldatov, An improved selection optimization method used for the measurement of ZZ production under conditions of ATLAS experiment during LHC run II, Phys. Part. Nucl. **54**, 232 (2023).
[82] C. Bonilla, D. Sokolowska, N. Darvishi, J. L. Diaz-Cruz, and M. Krawczyk, IDMS: Inert dark matter model with a complex singlet, J. Phys. G **43**, 065001 (2016).
[83] E. Barradas-Guevara, J. L. Diaz-Cruz, O. Félix-Beltrán, and U. J. Saldana-salazar, linking LFV Higgs decays $h \to \ell_i \ell_j$ with CP violation in multi-scalar models, arXiv:1706.00054.
[84] N. Khan and S. Rakshit, Study of electroweak vacuum metastability with a singlet scalar dark matter, Phys. Rev. D **90**, 113008 (2014).
[85] G. Cynolter, E. Lendvai, and G. Pocsik, Note on unitarity constraints in a model for a singlet scalar dark matter candidate, Acta Phys. Pol. B **36**, 827 (2005).
[86] M. Cepeda *et al.*, Report from Working Group 2: Higgs physics at the HL-LHC and HE-LHC, CERN Yellow Rep. Monogr. **7**, 221 (2019).
[87] M. A. Arroyo-Ureña, R. Gaitán, and T. A. Valencia-Pérez, SpaceMath version 1.0 a Mathematica package for beyond the standard model parameter space searches, Rev. Mex. Fis. E **19**, 020206 (2022).
[88] Search for elusive "di-higgs production" reaches new milestone. https://atlas.cern/updates/briefing/new-milestone-di-Higgs-search.
[89] G. Aad *et al.* (ATLAS Collaboration), Search for Higgs boson pair production in the two bottom quarks plus two photons final state in pp collisions at $\sqrt{s} = 13$ TeV with the ATLAS detector, Phys. Rev. D **106**, 052001 (2022).
[90] A. M. Sirunyan *et al.* (CMS Collaboration), Search for a heavy Higgs boson decaying to a pair of W bosons in proton-proton collisions at $\sqrt{s} = 13$ TeV, J. High Energy Phys. 03 (2020) 034.
[91] R. L. Workman *et al.* (Particle Data Group), Review of particle physics, Prog. Theor. Exp. Phys. **2022**, 083C01 (2022).
[92] P. Mandrik (FCC Study Group), Prospect for top quark FCNC searches at the FCC-hh, J. Phys. Conf. Ser. **1390**, 012044 (2019).
[93] A. Alloul, N. D. Christensen, C. Degrande, C. Duhr, and B. Fuks, FeynRules 2.0—A complete toolbox for tree-level phenomenology, Comput. Phys. Commun. **185**, 2250 (2014).
[94] J. Alwall, R. Frederix, S. Frixione, V. Hirschi, F. Maltoni, O. Mattelaer, H. S. Shao, T. Stelzer, P. Torrielli, and M. Zaro, The automated computation of tree-level and next-to-leading order differential cross sections, and their matching to parton shower simulations, J. High Energy Phys. 07 (2014) 079.
[95] T. Sjöstrand, S. Ask, J. R. Christiansen, R. Corke, N. Desai, P. Ilten, S. Mrenna, S. Prestel, C. O. Rasmussen, and P. Z. Skands, An introduction to PYTHIA 8.2, Comput. Phys. Commun. **191**, 159 (2015).

[96] J. de Favereau, C. Delaere, P. Demin, A. Giammanco, V. Lemaître, A. Mertens, and M. Selvaggi (DELPHES 3 Collaboration), DELPHES 3, A modular framework for fast simulation of a generic collider experiment, J. High Energy Phys. 02 (2014) 057.
[97] T. Plehn, Lectures on LHC physics, Lect. Notes Phys. **844**, 1 (2012).
[98] A. Pak, M. Rogal, and M. Steinhauser, Production of scalar and pseudo-scalar Higgs bosons to next-to-next-to-leading order at hadron colliders, J. High Energy Phys. 09 (2011) 088.
[99] D. de Florian *et al.* (LHC Higgs Cross Section Working Group), Handbook of LHC Higgs cross sections: 4. Deciphering the nature of the Higgs sector, arXiv: 1610.07922.
[100] ATLAS Collaboration, Performance assumptions based on full simulation for an upgraded ATLAS detector at a High-Luminosity LHC, Report No. ATL-PHYS-PUB-2013-009, 2013.
[101] A. M. Sirunyan *et al.* (CMS Collaboration), Identification of heavy-flavour jets with the CMS detector in pp collisions at 13 TeV, J. Instrum. **13**, P05011 (2018).
[102] G. Cowan, Discovery sensitivity for a counting experiment with background uncertainty, Technical report, Royal Holloway (U.K) University of London.